University of Vermont
ScholarWorks @ UVM

Graduate College Dissertations and Theses | Dissertations and Theses

2016

A Preliminary Study On The Interfacial Strength Of Red Abalone

Saleh Jaman Alghamdi
University of Vermont

Follow this and additional works at: https://scholarworks.uvm.edu/graddis

 Part of the Civil Engineering Commons

Recommended Citation
Alghamdi, Saleh Jaman, "A Preliminary Study On The Interfacial Strength Of Red Abalone" (2016). *Graduate College Dissertations and Theses*. 633.
https://scholarworks.uvm.edu/graddis/633

This Thesis is brought to you for free and open access by the Dissertations and Theses at ScholarWorks @ UVM. It has been accepted for inclusion in Graduate College Dissertations and Theses by an authorized administrator of ScholarWorks @ UVM. For more information, please contact donna.omalley@uvm.edu.

A PRELIMINARY STUDY ON THE INTERFACIAL STRENGTH OF RED ABALONE

A Thesis Presented

by

Saleh J Alghamdi

to

The Faculty of the Graduate College

of

The University of Vermont

In Partial Fulfillment of the Requirements
for the Degree of Master of Science
Specializing in Civil Engineering

October, 2016

Defense Date: June 14, 2016
Thesis Examination Committee:

Ting Tan, Ph.D, Advisor
Jie Yang, Ph.D., Chairperson
George Pinder, Ph.D.
Cynthia J. Forehand, Ph.D., Dean of the Graduate College

Abstract

Nacre is a hierarchical material found within the tough shells of red abalone. Despite being composed of calcium carbonate, nacre exhibits remarkable mechanical properties resulting from the nanoscale brick-and-mortar structure made from aragonite polygons. The objective of this research is to elucidate the toughening mechanisms associated with the interfacial resistance of red abalone. This was achieved by studying the mechanical behavior of dry nacre under pure shear and tension, and characterizing the associated fracture mechanisms using optical and scanning electron microscopes. Mathematical modeling was applied to further quantify the contribution of protein chains, nano-asperities and shear pillars to interfacial strengths. Preliminary conceptual models were proposed to elucidate the toughening mechanisms of polymorphic aragonite structures in red abalone. The findings can extend our understanding of the mechanical behavior of natural materials and promote the research and development of high performance bioinspired materials.

ACKNOWLEDGEMENTS

Firstly, I would like to express my sincere gratitude to my advisor Prof. Ting Tan for his endless support, patience, motivation, and immense knowledge. His guidance has been a critical factor in my ability to do research and enjoy doing it. Besides my advisor, I would like to thank the rest of my thesis committee: Prof. George Pinder and Prof. Jie Yang, not only for their insightful comments and valuable guidance, but also for their hard questions which driven me to broaden my scope of knowledge. I would like to acknowledge the help and collaboration of Dr. Tian Xia and Dr. Dryver Huston. I also would like to take this opportunity to express sincere gratitude to my parents and my sisters for their unceasing encouragement and support. I would particularly like to thank my friend Mousa Amery and the members of my research group, Christopher Hale-Sills, Yujie Li and Zhuang Liu who helped and supported me throughout this venture. My sincere thanks also goes to Michele von Turkovich who gave me access to the Scanning Electron Microscope at the University of Vermont. Without her precious support I would not be able to take some great SEM images. I also would like to thank Floyd Vilmont, for his continuous assistance throughout the research involved in this thesis. Finally, I would like to express my appreciation to Taif University for giving me this scholarship.

TABLE OF CONTENTS

Contents Page

LIST OF TABLES

Table page

LIST OF FIGURES

INTRODUCTION

Structural materials found in nature exhibit excellent mechanical properties such as high toughness and strength (Dunlop et al., 2010; Wegst et al., 2004). A great example is nacre, which is a biological composite that can be found in the inner layer of many shells such as oysters and abalones (Jackson et al., 1988). As can be seen in Figure 1, nacre is comprised of a hierarchical structure consisting of tightly stacked and organized polygonal aragonite platelet layers of thickness of ~0.5 μm. A thin layer of bio-polymers 20-50 nm composed mainly of proteins is sandwiched between the aragonite tablets (Song et al., 2003). The brittle aragonite platelets occupy around 95% of the volume of nacre, where the remaining 5% is occupied by the organic layer (Ji et al., 2004). In addition, it is reported that nacre is 3000 times tougher than its fragile constituent, i.e., calcium carbonate ($CaCO_3$) (Barthelat et al., 2007). A closer look at the microstructure of nacre shows other nanoscale structural features that contribute to the high toughness of nacre. These mechanisms include: (I) Interlocking mechanisms resulting from nano-aspertities contacts; (II) Sheer pillars, i.e., mineral bridges with diameter of ~50 nm that connect the vertically adjacent tablets (Sun et al., 2012). Shear Pillars enhance the stiffness, the strength and the fracture toughness of nacre (Song et al., 2003); and (III) The inter-pallet polymers (proteins) that have substantial roles in nacre's high fracture toughness (Smith et al., 1999, Barthelat et al., 2007). These mechanisms are illustrated in Figure 2. Furthermore, the structure of nacre contains what is known as growth layers (Sumitomo et al., 2011; Su et al., 2002; Lin et al., 2008), which are layers of alternating aragonitic and organic structures in the shell, as shown in Figure 3. The aragonitic components within the growth layers include both

columns and spherulites that are harder than nacre (Sumitomo et al., 2011; Su et al., 2002). In this work, the hybrid toughening mechanisms of alternating polymorphic structures in red abalone were studied using an integrated experimental and analytical approach. In particular, this thesis examined the interfacial behavior of nacreous tablets under pure shear and tension. Further, conceptual models were proposed to elucidate the structural roles of different aragonite components in red abalone. Additionally, FEM studies were conducted to quantify contributions of individual toughening mechanisms to the interfacial shear strength of nacre.

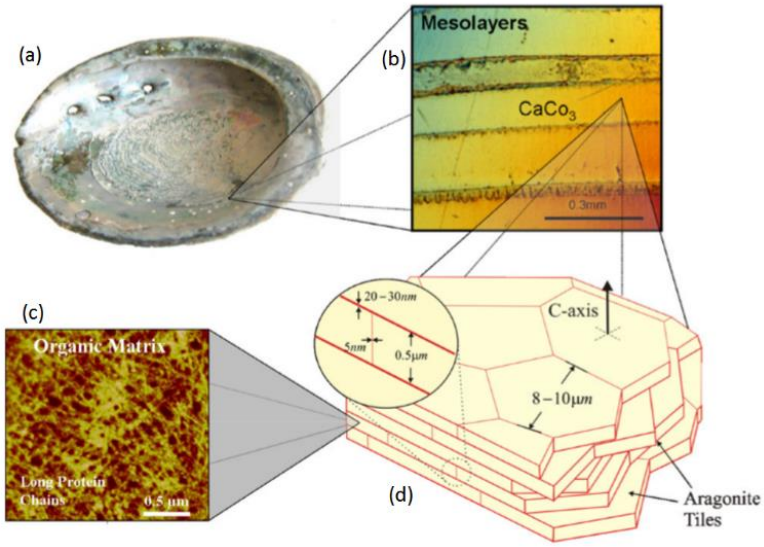

Figure 1 : An overall view of hierarchical structure of abalone shell. (a) an abalone shell; (b) nacreous structure and mesolayers; (c) the organic matrix between mineral tablets; and (d) the mineral tablets (Meyers et al., 2008).

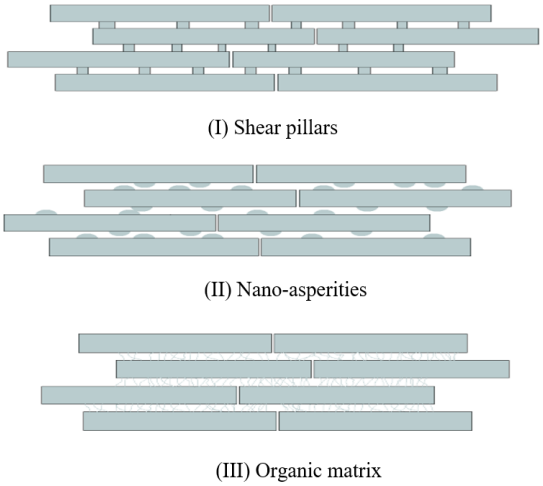

Figure 2: A schematic showing the three toughening mechanisms of nacre.

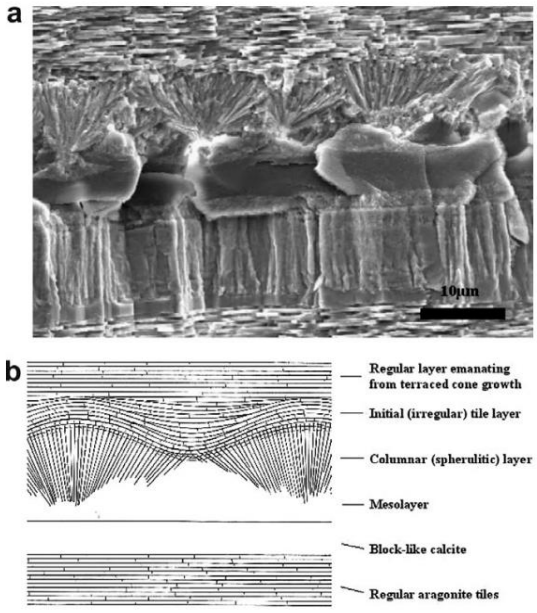

Figure 3: Cross-sectional view of growth interruption: (a) SEM and (b) schematic diagram (Lin et al., 2008).

1.2 Motivation

In the past three decades, nacre has been extensively studied using a variety of experimental, analytical and numerical approaches. Despite these efforts, limited research exists to quantify the inter-pallet shear behavior of nacre, and to understand how abalones resist external loads through their polymorphic aragonite layers, i.e., the alternating nacreous and growth layers. Thus, we apply an integrated experimental and analytical approach to explore these questions.

1.3 Research Objectives

The research objective of this study is to use integrated experimental and computational modeling approaches to elucidate the mechanical behavior of polymorphic aragonite structures in red abalone;

- Study the interfacial shear strengths of nacre in red abalone under pure tension and shear
- Characterize the fracture mechanisms of red abalone under pure shear and tensile stresses
- Conduct a finite elements study to quantify the contributions of inter-pallet polymers, nano-asperities contact and sheer pillars to the interfacial shear strengths of nacre.

LITERATURE REVIEW

2.1 Red Abalone

The red abalone (Haliotis rufescens), is a species of a large sea snail with the following taxonomic hierarchy (ITIS, 2016)

Table 1: Taxonomic hierarchy of red abalone.

Kingdom	Animalia
Subkingdom	Bilateria
Infrakingdom	Protostomia
Superphylum	Lophozoa
Phylum	Mollusca
Class	Gastropoda
Subclass	Prosobranchia
Order	Archaeogastropoda
Family	Haliotididae
Genus	Haliotis
Species	Haliotis rufescens

The red abalone, shown in Figure 4, can be found along the west coast of North America. Their habitat is described as rocky and abundant with seaweeds. The depth of their habitat ranges from intertidal zone to 100-foot-deep in water. For food, they essentially consume two types of seaweeds, i.e., bull kelp and giant kelp (University of California, 2016). In their environment, abalone encounters myriad dangers, such as attacks from predators, whirlpools, heavy falling objects and other ocean threats. Therefore, these animals have evolved over the years and adapted a proper protection in the form of a shell (RBML, 2011). The shell is large and thick, and can reach a maximum of 12.2 inches, which makes it the largest species of abalone in the world (RBML, 2011). The shell's outer surface is pinkish or brick red possessing a rough and wavy characteristic and contains a few respiratory pores. The shell interior is iridescent with a large, oval muscle scar

(University of California, 2016). The red abalone shell was specifically selected to be studied in this thesis for two reasons: (I) The large size and thickness of the shell which makes sample preparation more consistent; and (II) The shell's widespread usage in scientific research allows us to compare our findings to prior results.

Figure 4: The red abalone in it natural habitat. (SIMoN,2016)

2.1.1 Red Abalone Shell Composition

Red abalone shells essentially comprise of two basic components; calcium carbonate and proteins. The calcium carbonate components include both aragonite and calcite. The two minerals are discussed in the following sections.

2.1.1.1 Aragonite

Aragonite is the second most common polymorph of natural calcium carbonate ($CaCO_3$). It is metastable and can transform to calcite due to the environmental changes.

Its morphology can be described as; Short to long prismatic [100], flattened {010}; acicular or tabular {001} (Mindat,2016). Aragonite has a strength of 30 MPa. Its elastic modulus ranges between 80 and 205 GPa along different crystallographic directions (Currey, 1977; Barthelat et al., 2007; Jackson et al., 1988; Bass et al., 1995; Ji et al., 2004). The crystal structure of aragonite is shown in Figure 6a and 6b.

2.1.1.2 Calcite

Calcite is another polymorph of calcium carbonate ($CaCO_3$). It is more common and abundant than aragonite. In fact, over 800 different forms have been documented. Calcite exhibits a relatively low Mohs hardness, and has different strengths depending on the crystallographic orientations (Mindat,2016). The crystal structure of calcite is shown in Figure 6c and 6d.

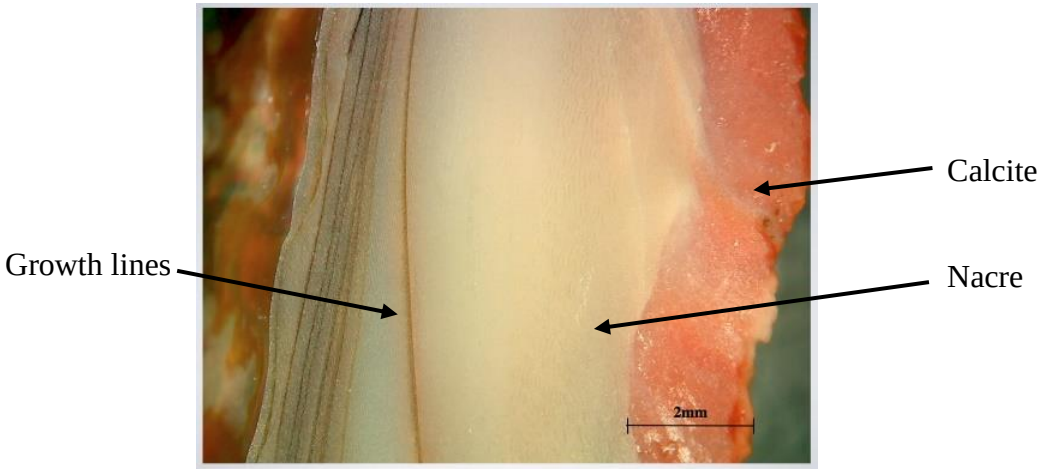

Figure 5: The image shows a cross section of a piece of red abalone shell. The middle beige section is nacre, and the outer red portion is calcite. The cross section also shows some growth lines.

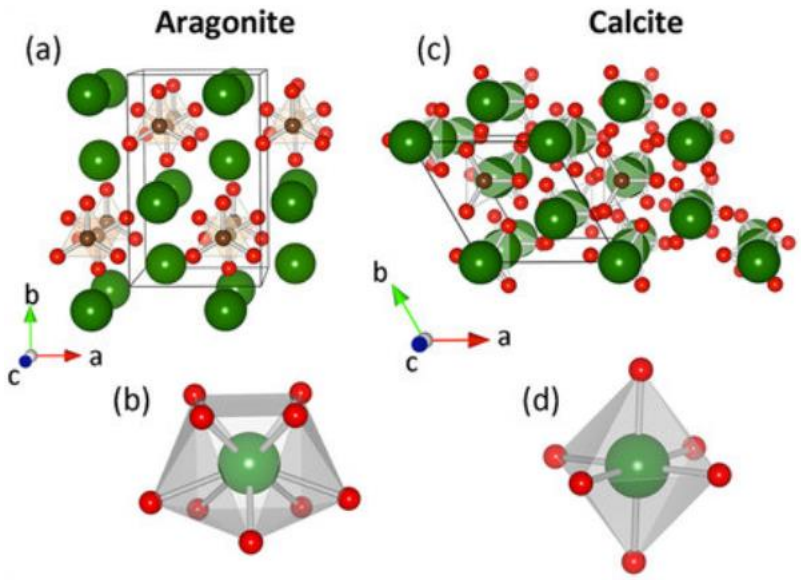

Figure 6: (a) and (b) show the crystal structure of Aragonite; (c) and(d) show the crystal structure of calcite (Soldati et al., 2016).

2.1.2 Nacre

The red abalone uses calcium carbonate and proteins to build a tough microstructure called nacre. Nacre is mostly comprised of aragonite, with a small fraction of organic materials (Currey, 1974). Nacre makes up the inner layers of most gastropod and bivalve seashells, and is known for its iridescence and excellent mechanical properties. The microstructure of nacre can be described as microscopic aragonite polygons arranged and tightly stacked in layers to form a brick-and-mortar structure. While the bricks are made of aragonite tablets, the mortar is an organic matrix made primarily of proteins.

2.1.2.1 Aragonite Tablets

The aragonite tablets are made of calcium carbonate ($CaCO_3$), and are tightly stacked to form a brick-and-mortar structure, as seen in Figure 7. Each “brick” is a polygonal tablet that is ~0.5 μm thick and 5-8 μm in diameter. Each tablet has core overlap

areas with both the top and bottom layers, and another overlap with the adjacent tablets. The inter-column overlap areas cover about 1/3 of the surface area of the tablet layers (Barthelat, et al., 2007). Nano-indentation studies by Barthelat et al. (2006) showed that the elastic properties of nacre tablets are very similar to those of single-crystal aragonite minerals. Nevertheless, tablets exhibit higher strengths than the documented values for aragonite. Li et al. (2004) also used indentation and atomic force microscopy to investigate the deformation behavior of nacre. In that study, micro-indentations were performed to induce cracks in a polished sample from an abalone shell. It was shown that radial cracks initiated and propagated along the interfaces of nacreous tables in a zigzag manner. More importantly, plastic deformations in the aragonite tablets were observed around the crack tips. They showed that aragonite platelets are not entirely brittle but ductile, resulting from the presence of nano-grains. Young's modulus of the tablets reported in literature ranged from 50 GPa (Okumura et al., 2001), 70 GPa (Evans et al., 2001) to 100 GPa (Jackson et al., 1988).

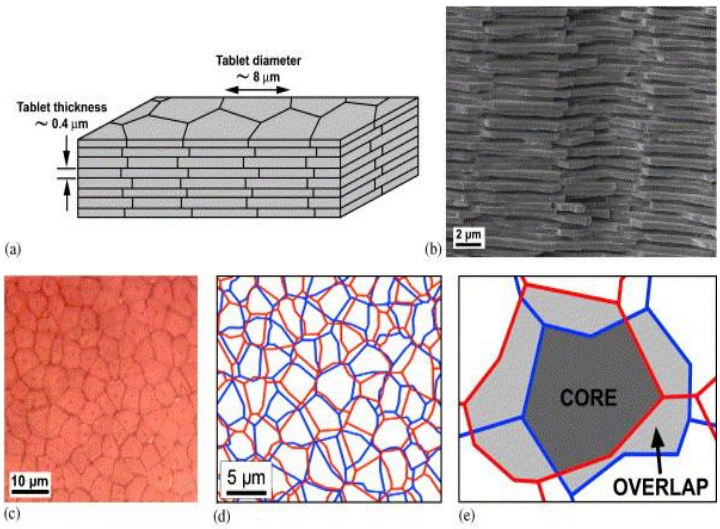

Figure 7: Nacreous structures, (a) a schematic of the tablets arrangement showing the brick-and-mortar structure of nacre; (b) an SEM image of a fracture surface in nacre; (c) top view of tablet tiling in nacre; (d) the reconstitution of tablets from one layer to the next; and (e) core and overlap areas in the tablet arrangements (Barthelat et al., 2007).

2.1.2.2 Organic Matrices (Mortar)

Besides aragonite, nacre contains 5% (by volume) organic matter, found between the tablets with a thickness of ~30 nm, as shown in Figure 8. The main constituent of the organic layer is protein, particularly, fibrous β-chitin network, gel-like silk fibroin protein and glycoproteins (Weiner, 1979; Sumitomo et al., 2008). The organic matrices contribute essentially to the mechanical behavior of nacre. Evans et al. (2001) reported that the organic macromolecules (protein lustrin A in abalone nacre) make nacre tougher by working as a viscoelastic adhesive at the interfaces between tablets. Smith et al. (1999) showed that when the adhesive protein chains are stretched, saw-tooth pattern manifests in the force-extension curves (Figure 9), indicating that the structures unfold or the sacrificial bonds break. This deformation mechanism of the matrix ligaments was demonstrated by a

transmission electron microscopy (TEM) study by Sumitomo et al. (2008). Furthermore, Ghosh et al. (2007) showed how proximity of aragonite tablets affects the unfolding mechanisms of proteins when pulled. According to their study, the amount of work needed to unfold proteins is considerably higher when protein domain is close to the aragonite tablets. Jackson et al. (1988) determined the shear strength of the organic matrix to be 37 MPa, with shear moduli of 1.4 GPa for wet organic matrix and 4.6 for a dry one; whereas a shear modulus value of 0.8 GPa was analytically reported by Barthelat et al. (2006).

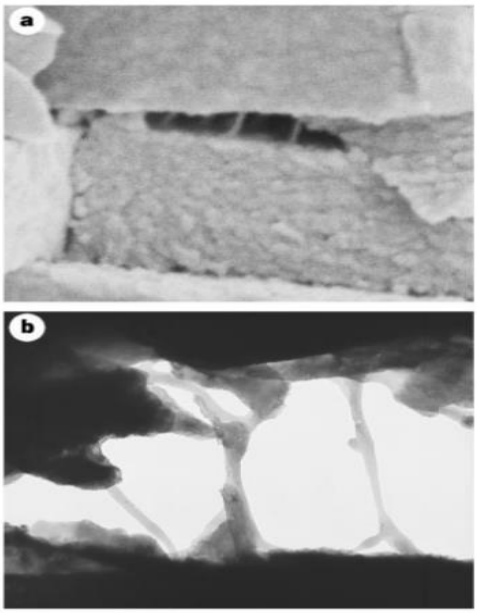

Figure 8: Scanning and transmission electron micrographs of a freshly cleaved abalone shell, showing adhesive ligaments formed between nacre tablets (Smith et al., 1999).

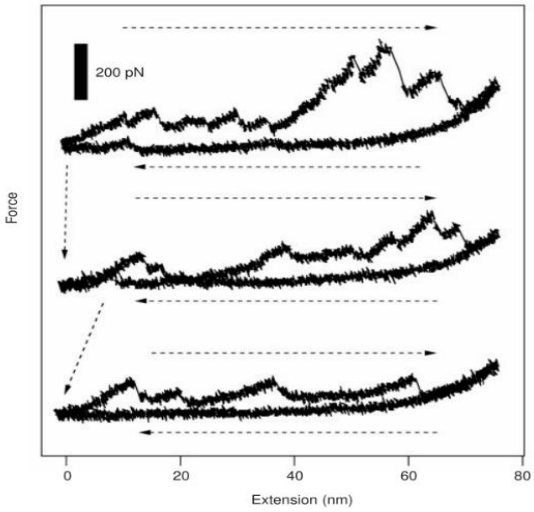

Figure 9: Consecutive force–extension curves, obtained using an atomic force microscope, due to pulling on a freshly cleaved abalone nacre surface (Smith et al., 1999).

2.1.2.3 Nano-asperities

Nano-asperities exist on the faces of the aragonite pallets (Figure 10), that are ~50 nm in diameter and 10-30 nm in height (Meyers et al., 2008; Checa et al. 2011). The density of asperities on the tablets determined by Song et al. (2001, 2002) is ~105/μm^2. Furthermore, asperities contribute to nacre's mechanical behavior by providing a mechanical interlocking mechanism that resists the interfacial sliding (Evans et al. 2001; Wang et al. 2001).

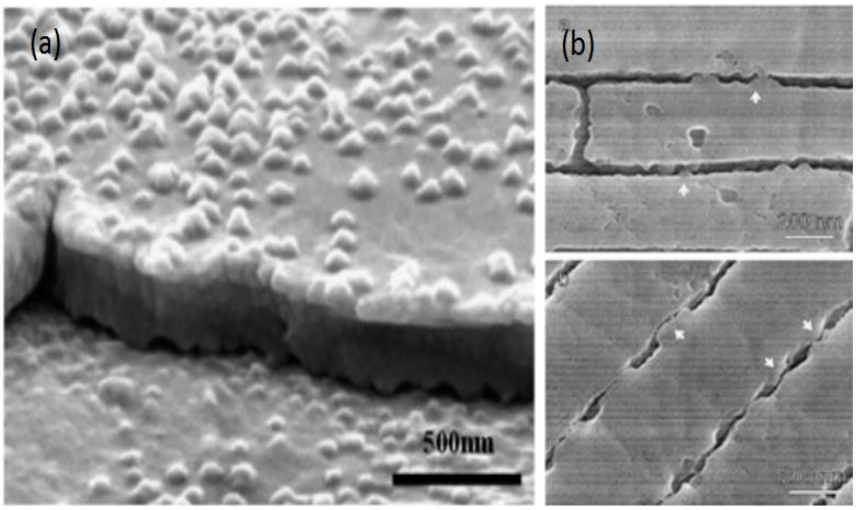

Figure 10: Nano-asperities on a red abalone tablet. (a) asperities on the surface of one tablet; (b) a side view of nacreous structure showing asperities in the interface of tablets (Meyers et al., 2008).

2.1.2.4 Shear Pillars (mineral bridges)

Other components present on the surface of the aragonite tablets are the mineral bridges (also known as shear pillars). In Figure 11, mineral bridges are described as roughly circular pillars with diameters of ~50 nm and heights of ~30 nm. By treating the organic matrix sheet as a fiber-reinforced composite, consisting of an organic matrix and fibers of the inorganic mineral bridges, Song et al. (2002, 2003) showed that the interfaces between tablets are five time stronger in resisting fracture when shear pillars are present in the interface. By performing three-point bending tests, they showed that cracks advance only along the interfaces and then the get arrested due to the presence of shear pillars in the interfaces. Song et al. (2001, 2002, 2003) determined the density of mineral bridges on an aragonite platelet layer to be ~91-116 /μm^2. In addition, they reported that the pillars are more abundant in the central region of the tablet than the outer one.

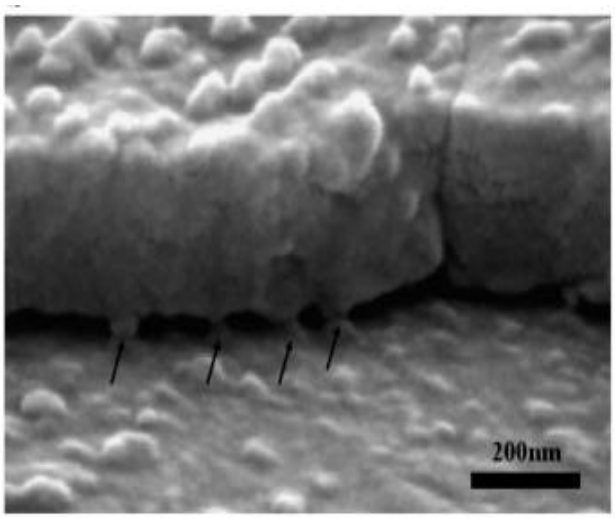

Figure 11: Shear pillars in the interface between tablets (Meyers et al., 2008).

2.1.2.5 Growth Layers

The red abalone shell is comprised mostly of nacre (Sumitomo et al., 2011). However, non-nacreous layers have been reported in literature (Erasmus et al., 1994; Sumitomo et al., 2011; Menig et al., 2000; Su et al., 2002; Lin et al. 2005). These layers are described as thin bands that constitute an organic and inorganic lamellar structure at the micro scale, as shown in Figure 12. The inorganic constituents include columns and spherulites (Erasmus et al., 1994; Su et al., 2002). Sumitomo et al. (2011) performed a nano-indentation study on the growth layer of abalone nacre and showed that the block-like and particle layers have similar mechanical properties as geological aragonite but exhibit higher strength than nacre itself. They also demonstrated that abalone possesses the ability to control the bio-mineralization processes based on seasonal lifecycles. In addition, Lin et al. (2005) showed that growth lines are efficient in deflecting cracks between nacreous structures. Further, Su et al. (2002) investigated the structure of growth layers in

abalone shell using X-ray diffractions, scanning electron microscopy (SEM) and transmission electron microscopy. They confirmed that the growth lines consist of blocklike and a spherulitic microstructures separated by an interlayer of organic matrices. They also reported that blocklike and spherulitic structures are comprised of the same mineral that constitutes the tablets in nacreous structure, i.e., aragonite.

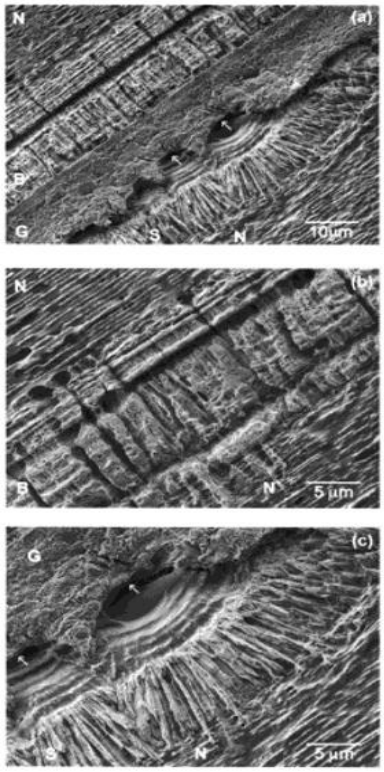

Figure 12 (a) Cross-sectional SEM images of the growth layers in red abalone; (b) a growth line in the absence of green protein layer and spherulitic layer; and (c) a closer look at the spherulitic structure. N, nacreous microstructures; B, blocklike microstructures; G, green organic matrices; S, and spherulitic microstructures (Su et al., 2002),

2.2 Previous Work

2.2.1 Mechanical Tests

Numerous mechanical experiments have been performed on nacre to characterize its mechanical properties. The following section briefly summarizes these experiments.

2.2.1.1 Compression and Tension Tests

Jackson et al. (1988) determined the tensile strength of nacre to be ~140 MPa for wet nacre and ~170 MPa for dry nacre. Barthelat et al. (2006) preformed tensile tests on dog-bone shaped samples of red abalone nacre and showed that nacre has elastic moduli of 70 and 90 GPa for wet and dry nacre, respectively. Tests by Wang et al. (2001) show that when abalone nacre is tested in tension parallel to the tablets, it exhibits an elastic behavior up to a strain of about 0.15%, then continues on a steady-state stress of at least 100 MPa until failure, which occurred at strain of roughly 1%. They explained that the inelastic strain is due to the dilatation bands occurring at the interpallet boundaries in addition to the interfacial sliding. However, in compression along the tablets, nacre shows a brittle behavior until failure, as can be seen in Figure 13. Furthermore, Barthelat et al. (2006) studied nacre under compression across the tablets and demonstrated that it possesses an average strength of 450 MPa, see Figure 14.

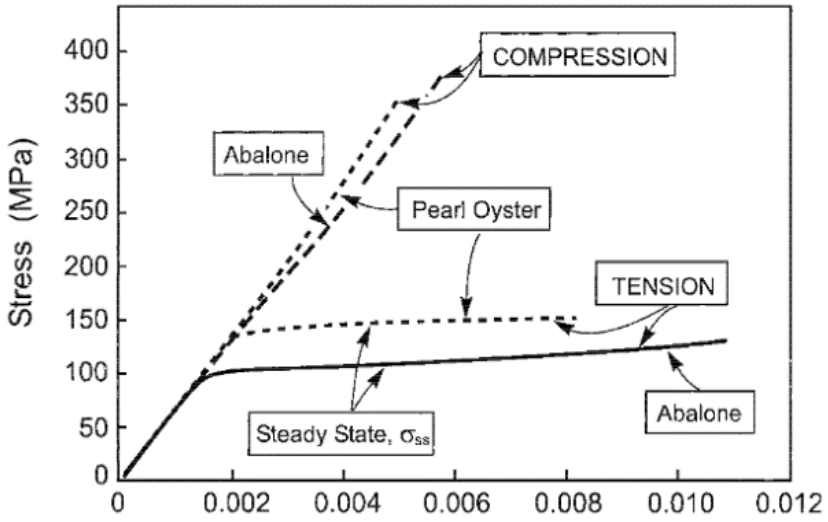

Figure 13: Stress–strain curves for nacre and pearl oyster in tension and compression (Wang et al., 2001).

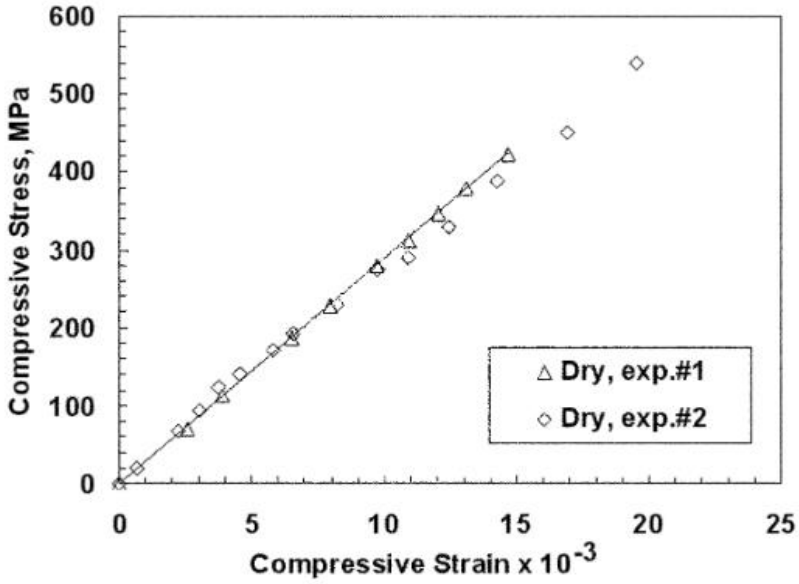

Figure 14: Compressive stress strain curves of nacre across the tablets (Barthelat et al., 2006).

Barthelat et al. (2007) also tested nacre in tension along the tablets and observed that when nacre is dry, it acts like a brittle material and fails when tensile stress reaches an

average of about 114 MPa, a value close to the tensile strength of pure aragonite. Wet nacre, on the other hand, shows an elastic behavior up to a strain of roughly 0.0006, then exhibits inelastic deformation until failure (Figure 15). Furthermore, Barthelat and Espinosa (2006) tested nacre in tension across the tablets and reported that it exhibits a strength of 15 MPa.

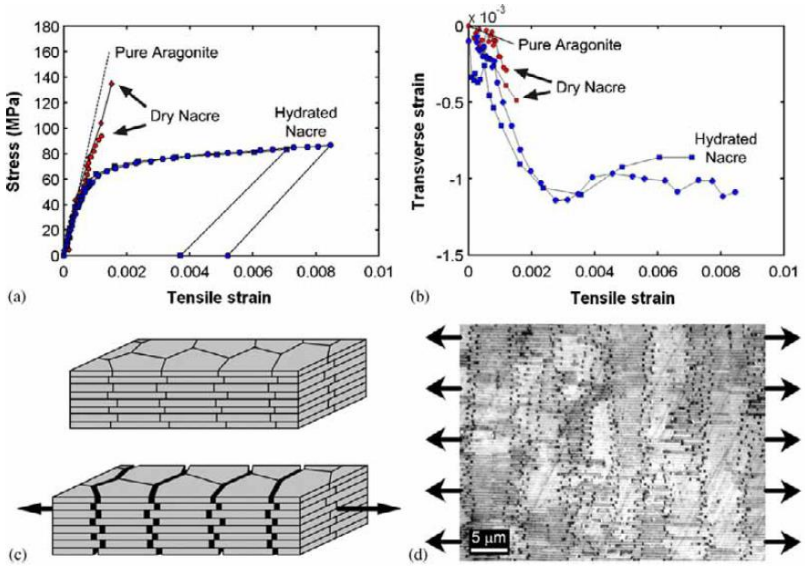

Figure 15: (a) Stress–strain curves of nacre in tension along the tablets; (b) the transverse strain versus the longitudinal strain; (c) schematics showing tablet sliding. The separation generates voids at the boundaries of the tablets; and (d) an SEM micrograph of a tensile specimen showing that all the potential sliding sites activated. The dark spots are voids generated by the tablet separation (Barthelat et al., 2007).

Nacre in red abalone was evaluated by Menig et al. (2000) under varying compressive loading rates and sample orientations. By preforming Weibull analyses with the fracture probability of 50%, they determined the compressive strength of nacre to be 235 MPa when the loading is quasi-static and is parallel to the tablets; and 540 MPa for loading direction perpendicular to the layers of tablets. In contrast, when the loading is dynamic, the compressive strength of nacre increases by about 50% to 548 MPa when tablet layers are parallel to the loading direction, and to 735 MPa when the layers are perpendicular to the compressive load. Stress-strain curves of this experiment are shown in Figure 16.

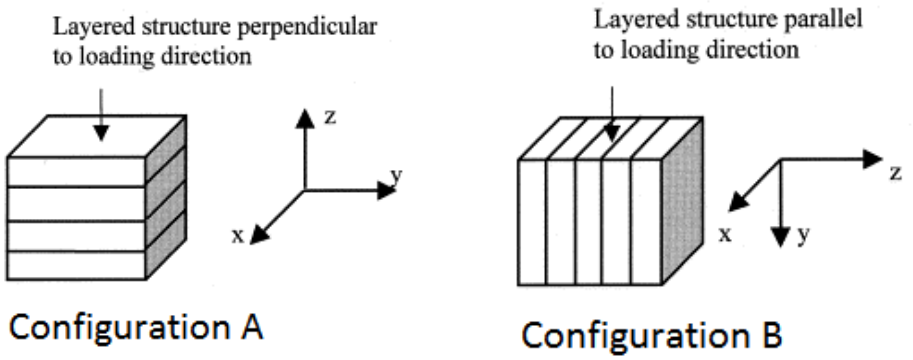

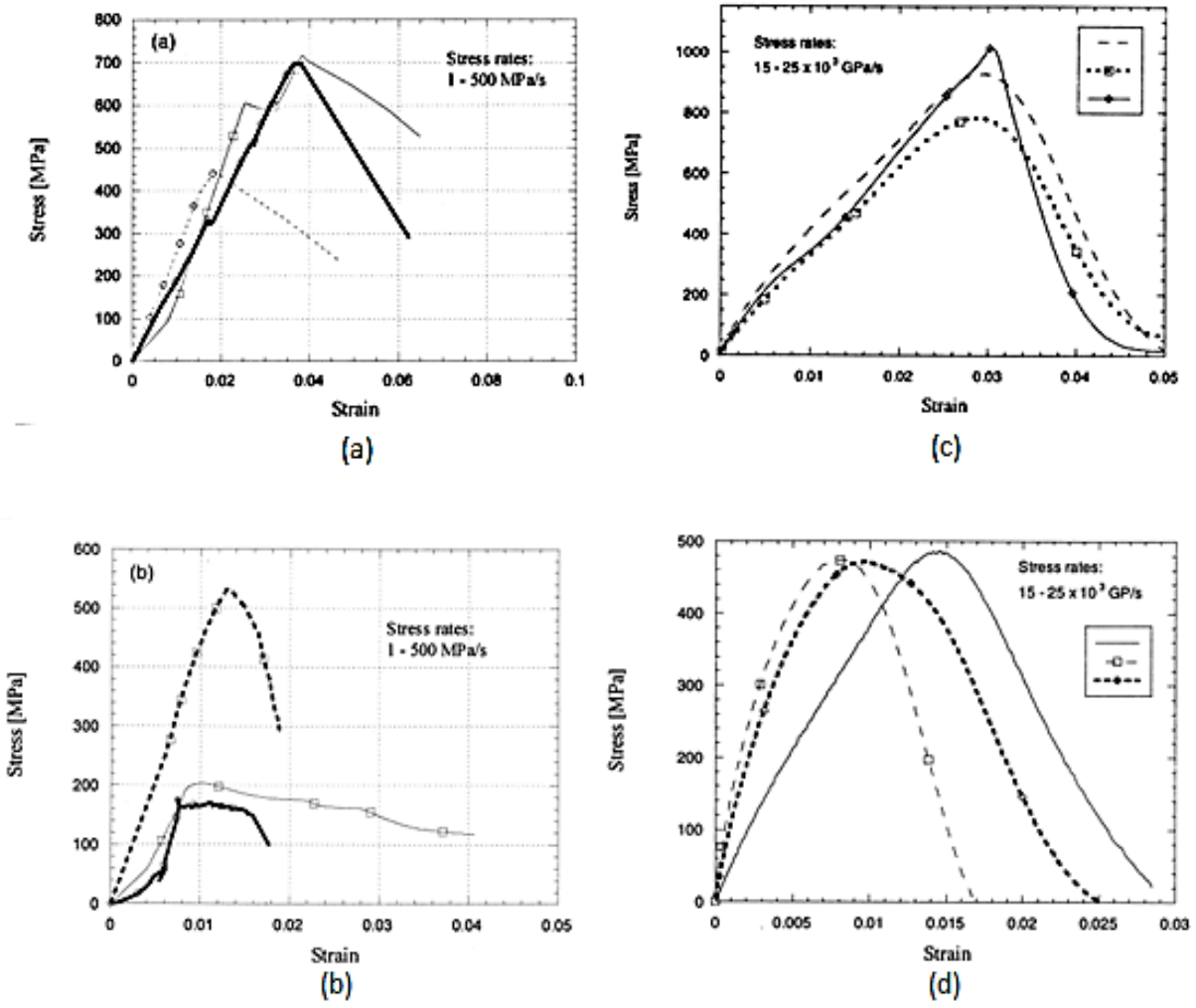

Figure 16 : Compressive stress–strain curves of abalone samples: (a) quasi-static, loading perpendicular to layered structure (configuration A); (b) quasi-static, loading parallel to layered structure (configuration B); (c) dynamic, loading perpendicular to layered structure (configuration A) and (d) dynamic, loading parallel to layered structure (configuration B) (Menig et al., 2000).

2.2.1.2 Bending Tests

To determine the flexural strength of nacre, several bending tests have been performed. Jackson et al. (1988) performed three-point bending experiments and reported

that dry nacre (E=70 GPa) from Pinctada shell is stiffer than wet nacre (E=60 GPa). Similar tests were conducted by Wang et al. (2001) on nacre samples taken from pearl oyster and red abalone. They showed that both flexural strength and Young's modulus of red abalone are higher when the orientation of the tensile surface is parallel to the lamellar boundaries (Figure 17).

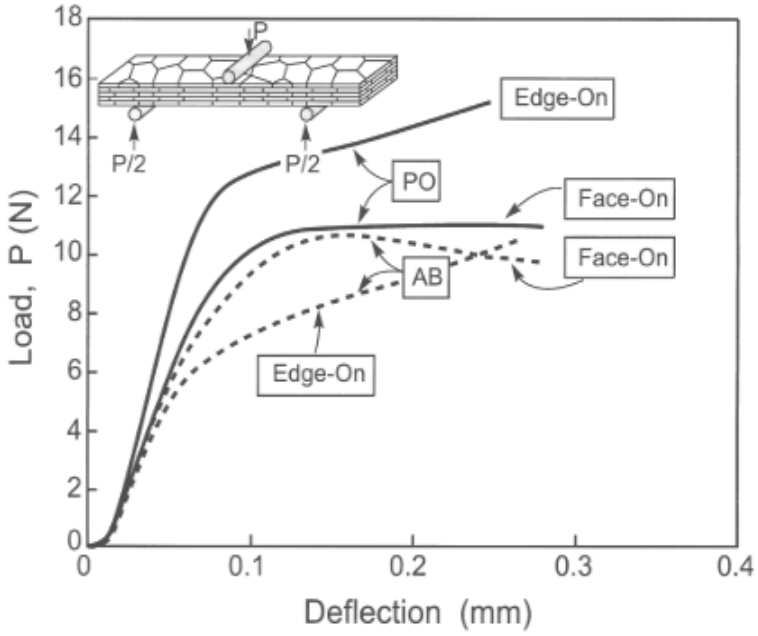

Figure 17: Load–deflection curves upon three-point bending. The insert indicates the face-on orientation with lamellar boundaries parallel to the tensile surface (Menig et al., 2000).

2.2.1.3 Fracture Tests

Nacre exhibits extraordinary fracture resistance. Many experiments have been performed on nacre to explore this unique property. Jackson et al. (1988) investigated nacre's work of fracture and reported that it ranges from 350 to 1240 J/m^2, depending on

the span-to-depth ratio and the degree of hydration. This value is 3000 greater than that of pure calcium carbonate. Sarikaya et al. (1990, 1992, 1994) tested single notched red abalone nacre samples using 3-point and 4-point bending tests and found that nacre has a fracture strength of 185 ± 20 MPa and a fracture toughness of 8 ± 3MPa $m^{1/2}$.

2.2.1.4 Shear Tests

Nacre was also tested in shear in prior studies. Menig et al. (2000) determined the shear strength by applying shear forces to cube-shaped samples of abalone. The applied load was parallel to the tablets layers of nacre (Figure 18), aiming at generating shear over a 2 mm gap in the sample. The stress-strain curves exhibited a segment up to 12 MPa, followed by another segment that increase steadily until failure (Figure 19). The shear strength of 30 MPa was obtained with the corresponding shear strain of 0.45.

Using a similar test set-up, Barthelat et al. (2007) investigated the interfacial shear behavior in wet and dry nacres under an optical microscope for strain measurements. The direct shear tests were performed on cube-shaped nacre samples (Figure 20). Test results of both dry and hydrated nacre showed an elastic region followed by an inelastic shear deformation and hardening. However, the yielding shear strengths of dry and wet nacre are 55 MPa and 20 MPa, respectively. In addition, shear moduli are 14 GPa and 10 GPa for dry and wet nacre, respectively. Furthermore, they reported that for both dry and wet samples, a considerable amount of expansion across the tablets occurred during the shearing process. They concluded that this is due to the presence of obstacles that tablets

climb up to slide. Additionally, combined shear and compression test was performed to study the impact of compressive stresses on the shearing resistance of dry and hydrated nacre. Results showed that albeit having a limited effect on the shearing resistance of wet nacre, compressive stresses cause dry nacre to exhibit higher shear strength.

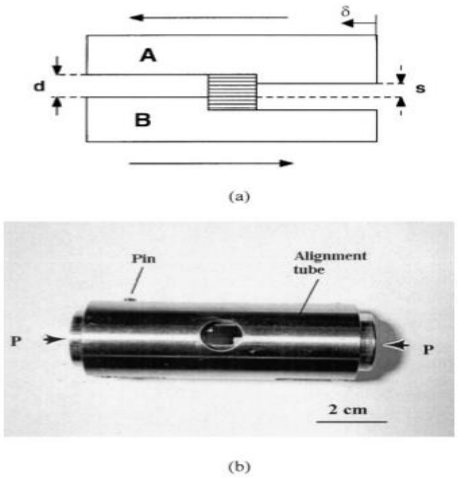

Figure 18: (a) A schematic of the direct shear test of the abalone shell; and (b) the actual shear testing device (Menig et al., 2000).

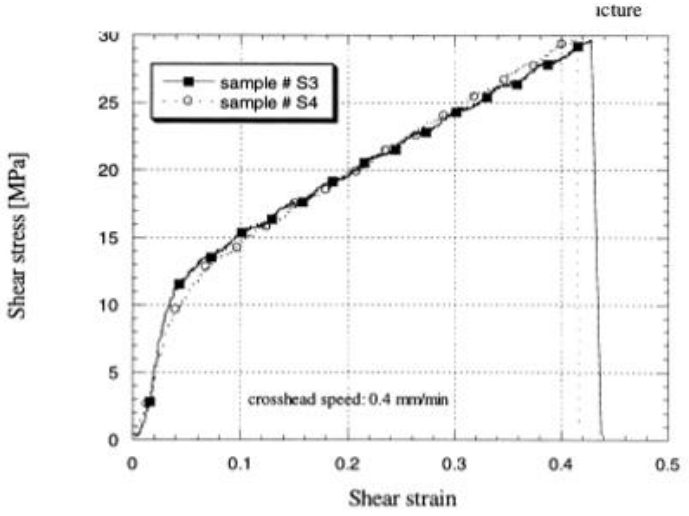

Figure 19: Stress-strain curves of abalone nacre samples after direct shear tests (Menig et al., 2000).

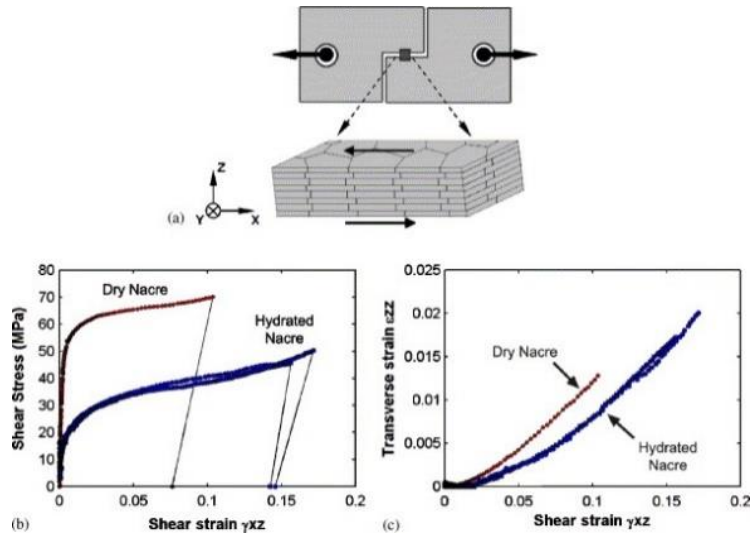

Figure 20: (a) The shear test configuration; (b) shear stress-strain curve and (c) shear strain curves in the transverse directions (Barthelat et al., 2007).

Lin et al. (2009) also evaluated the interfacial shear strength of abalone nacre using a similar set-up as the one used in Menig et al. (2000) but with a smaller gap. The distance was chosen to be 200 μm to ensure the shearing occurs in the nacreous regions between mesolayers and not slide across them. The shear strength measured was 36.9 ± 15.8 MPa with the corresponding shear strain of 0.3. As shown in Figure 21, the shear test results show an increment until failure.

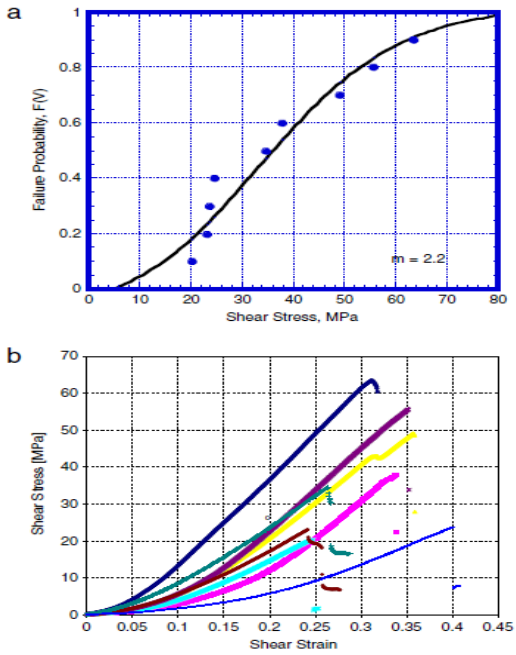

Figure 21: Direct shear tests with loading parallel to a layered structure: (a) The Weibull distribution of shear strengths and (b) stress–strain curves (Lin et al., 2009).

2.2.2 Finite Elements Studies

Beside mechanical experimentations, different numerical models have been used to understand the mechanical responses of nacre. Several approaches are briefly described hereunder.

Barthelat et al. (2007) developed a three-dimensional FEM model to study how tablet waviness affect the mechanical response of nacre. In another study, Evans et al. (2001) used FEM models to investigate if nano-asperities, among other mechanisms, are responsible of the inelastic deformation observed in nacre. Their results indicated that nano-asperities contribute to the mechanical behavior of nacre by providing strain-hardening that is large enough to ensure that multiple dilatation bands are formed but not so large that tablets break internally. In addition, Katti et al. (2001, 2006) constructed three-

dimensional FEM models to simulate the overall mechanical behavior of nacre and investigate different toughening mechanisms. Furthermore, Dashkovskiy et al. (2007) studied the impact of the organic matrix incompressibility on the elastic modulus of the nacreous composite by simulating two-dimensional finite element in tension, shear and bending models. Additionally, Barthelat et al. (2006) modeled the inter-tablet interfaces in nacre. Their results suggested that nano-asperities are strong enough to resist tablet sliding and endure climbing, at least at early stages of deformation.

2.2.3 Analytical Models

Several analytical models were also developed to understand the mechanical behavior of nacre. For instance, Kotha et al. (2001) developed a two-dimensional shear lag model to analyze how stresses transfer between the aragonite platelets. Based on their results, it is suggested that in order to create high toughness nacre-like composites, the aspect ratio of the tablets should be small. Additionally, a two-dimensional micromechanical model was proposed by Bertoldi et al. (2008) to characterize the macroscopic behavior of nacre. They showed that it is important to take into consideration nacre's bimodularity and anisotropy for a proper interpretation of experimental data.

2.2.4 Large Deformation and Toughening Mechanisms of Nacre

The unique mechanical properties of nacre have attracted research attention over the past decades to understand the large plastic deformation observed in nacre's response and the corresponding toughening mechanisms which are described briefly hereunder.

Movement of the aragonite tablets and shearing of their interfaces contribute to the inelastic deformations observed in nacre's response (Wang et al., 2001; Jackson et al., 1988; Barthelat et al., 2007). Within the nacreous interfaces, nano-asperities provvide nano-scale strengthening as they provide interlocking mechanisms to resist tablet sliding (Wang et al., 2001; Barthelat et al., 2006; Evans et al. 2011). Shear pillars are another nano-scale toughening components on the tablet surfaces that can toughen the interfaces fivefold (Song et al. 2002 and 2003). After studying the nano-scale structures of abalone nacre, Li et al. (2004) suggested that nanograins strengthen nacre tablets and prevent them from breaking during the deformation. In another study, Barthelat et al. (2007) reported that the wavy nature of the tablets is responsible for the hardening and damage tolerance of nacre. Evans et al. (2001) showed that the organic macromolecules (protein lustrin A in abalone nacre) is what make nacre tough as they work as a viscoelastic adhesive at the interfaces between tablets. Smith et al. (1999) showed that when the adhesive protein is stretched, a sawtooth pattern manifests in the force-extension curve which is an indication that either the structural domains unfold or the sacrificial bonds break. This behavior of the proteinous interface contribute to the large plastic deformation observed in nacre's response. Other toughening mechanisms suggested by Sarikaya et al. (1990, 1992 and 1994) include: crack deflection, tablet pull out, and crack bridging.

2.2.5 Torsion

For this study, torsional tests are used to characterize the interfacial shear strength of the nacre. A pure shear stress distribution across the entire cross section of the sample is achieved under torsional loads (Tan et al., 2013). When torsional loads are applied, the

principal tensile stresses are oriented at 45 degrees relative to the loading axis (Figure 22). As in Figure 23, under torsion, ductile materials exhibit relatively flat fracture surfaces, while brittle materials exhibit helical fracture surfaces at 45 degrees relative to the cylindrical axis.

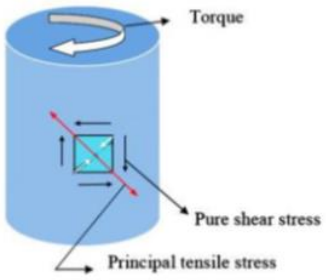

Figure 22: Illustrations of shear and principal tensile stresses induced by torsion.

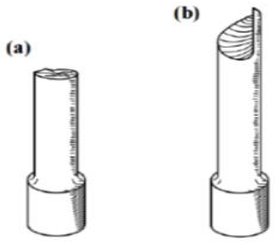

Figure 23: Two failure modes under torsion: (a) ductile material and (b) brittle material.

Unlike direct shear tests, torsional tests induce pure shear stresses in the cross section. In addition, the maximum shear stresses exist on the surface of the entire gauge length rather than a single point (Wang 2003). Once the interfacial shear strength is achieved along the circumference, the tests will end soon due to the shear gradient along the radius. Every cross section is subjected to the same shear stress distribution.

2.2.6 Tension

Tension tests were used in this work to characterize the tensile strength of red abalone. A tensile test is done by mounting the nacre dog-bone shaped sample in ADMET testing machine (ADMET, Norwood, MA) and then applying tensile force on the sample. The ultimate tensile strength is defined as the highest value of engineering stress, Figure 24. In the case of ductile materials, the point at which the deformation starts to localize (forming a neck) corresponds to the ultimate tensile strength (Figure 25a). Moderately ductile materials fracture before they necking is formed (Figure 25b). Brittle materials, on the other hand, do not yield before fracture (Figure 25c).

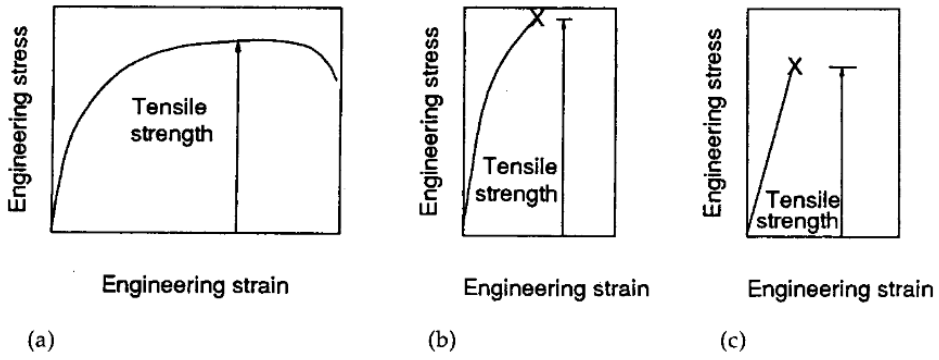

Figure 24: Stress-strain curves showing that the tensile strength is the maximum engineering stress regardless of whether the specimen necks (a) or fractures before necking (b and c). (Davis 2004)

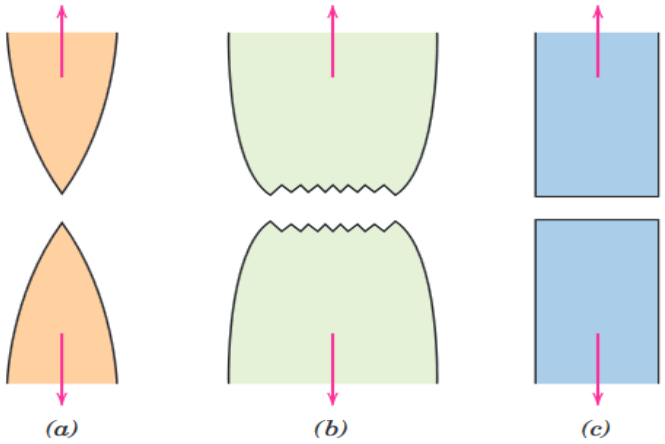

Figure 25: (a) Highly ductile fracture in which the specimen necks down to a point; (b) Moderately ductile fracture after some necking; and (c) Brittle fracture without any plastic deformation (Callister et al., 2007).

2.2.7 Mechanical Properties

Table 2: Upper and lower bounds of the reported mechanical properties of nacre and its constituents. Values in curly brackets are used by researchers in their models.

Young's modulus (GPa)				
Nacre [1,2]	Tablets[3,4]	Mineral Bridges [5,6]	Asperities[5]	Organic matrix[7,8]
70-90	100-{205}	{40}-100	{1.6}	0.02-{20}

Shear Modulus (GPa)				
Nacre[1]	Tablets	Mineral Bridges	Asperities	Organic matrix [9,9]
14	-	-	-	1.4 - 4.6

Poisson Ratio				
Nacre	Tablets[1,7]	Mineral Bridges	Asperities	Organic matrix[7]
-	{0.20} – {0.3}	-	-	{0.1 to 0.499}

References for mechanical properties presented in table 2:

1: Barthelat et al. (2007)

2: Lin et al. (2008)

3: Dashkovskiy et al. (2007)

4: Katti et al. (2005)

5: Askarinejad et al. (2015)

6: Song et al. (2003)

7: Barthelat et al. (2004)

8: Katti et al. (2001)

9: Jackson et al. (1988)

METHODOLOGY

3.1 Sample Preparation

A red abalone shell with a dimeter of ~8.5 inches, shown in Figure 26, was purchased from the Shell Shop (The Shell Shop, MA, USA). The shell was cleaned and then documented via photography. Preliminary measurements of the shell were taken using rulers and calipers. In addition, a three-dimensional computer-aided drafting (CAD) mesh was obtained by photographing the shell from every side using a digital camera (Cisco Systems, San Jose, CA). A free base version of Autodesk® ReCap 360 (Autodesk, San Rafael, CA) was then used to obtain a photorealistic, high-resolution three-dimensional CAD model of the shell.

Figure 26: Red abalone shell obtained for testing

The abalone shell was then cut into segments in the University of Vermont's Votey machine shop. Each segment was further cut into strips roughly 0.3 inches wide, and varying lengths. These strips were finally shaped to obtain 0.3 by 0.3 inches cube-shaped samples (Figure 27).

Figure 27: Cutting up the shell into segments (a), and then strips (b).

The cube edges were cast in horizontally-placed molds using Loctite Fixmaster Fast Cure Poxy Pak Epoxy (Henkel, Rocky Hill, CT). To ensure good bonding between the epoxy and samples, the edge surfaces were roughened using filing tools. Once cured, the epoxy parts in samples edges were squared to 0.3 × 0.3 inches using a Bridgeport style mill (Hardinge, Inc., Elmira, NY). A 0.079-inch medium diamond grinding pin was used in the Suburban Tool Spin (Suburban Tool, Auburn Hills, MI) to make the final dog-bone samples. The cutting was done manually by rotating the sample along its axis while a low speed spinning diamond pin cuts away the nacre samples' gauge sections. During cutting, the epoxy sections were gently clamped to reduce impacts on the nacre section.

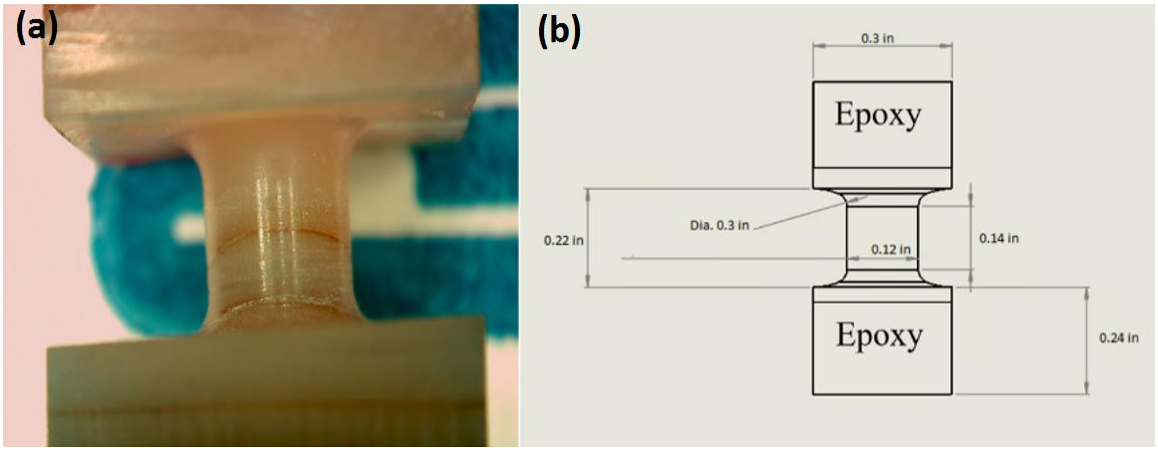

Figure 28: (a) A typical nacre dog-bone shaped specimen; and (b) the dimensioned drawing of a typical dog-bone shaped specimen.

The machining set-up is shown in Figure 29, in which a three-dimensional manipulator stage was used to accurately cut samples with consistent dimensions.

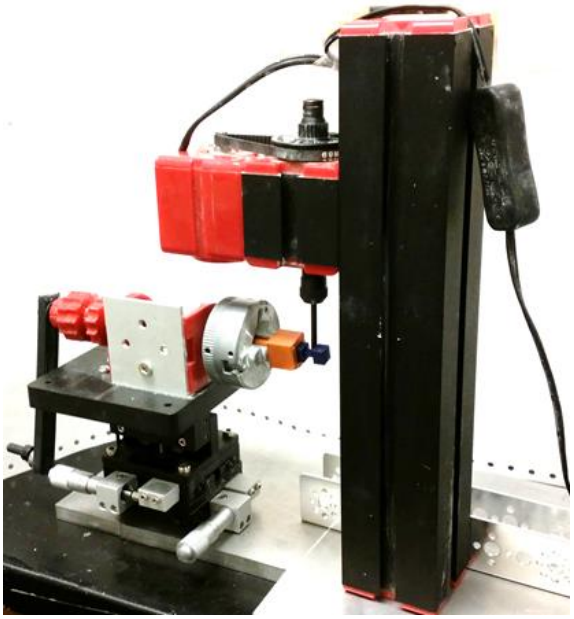

Figure 29: A photograph showing the apparatus used to make the dog-bone shaped nacre specimens.

Before testing, the dog-bone gauge sections were polished to eliminate stress concentration during the test. This was done by using sandpaper of grit-size varying from P240 to P400 (3M Company, Maplewood, Minnesota). Figure 30 shows images of a representative sample before and after polishing. Further, each sample's surface features, such as the numbers of growth lines and their angles, were carefully documented to assist in the postmortem fractography characterization. Samples dimensions are summarized in Table 3.

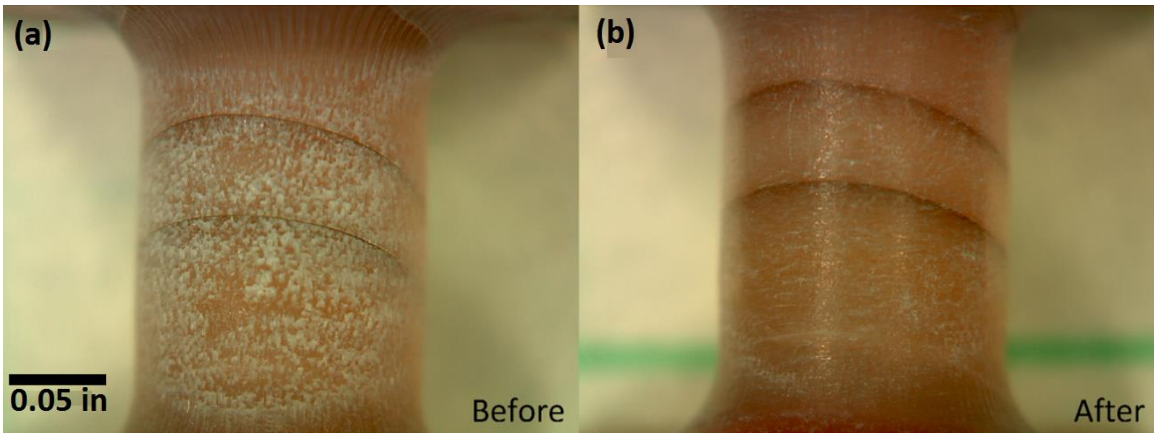

Figure 30: Two photographs of the nacre specimens before (a) and after polishing (b).

Table 3: Nacre samples dimensions and growth lines information.

Sample Id	Gauge length (Round to Round) (inches)	Diameter (inches)	Number of growth layers	Growth layers Angles (relative to the gauge section's axis)
1	0.181	0.138	3	~20 degrees
2	0.125	0.0935	3	~20 degrees
3	0.188	0.128	4	~32 degrees
4	0.140	0.138	4	~20 degrees
5	0.167	0.138	6	~12 degrees
6	0.172	0.140	5	~0-5 degrees
7	0.185	0.140	5	~17 degrees
8	0.171	0.1385	12	~0-1 degrees
9	0.144	0.139	3	~19 degrees
10	0.172	0.140	3	~18 degrees

In addition, aragonite crystal clusters were purchased from an internet supplier (Gold Nugget Miner). Dog-bone shaped samples were then prepared. The aragonite samples served as references, and their dimensions are summarized in Table 4 below.

Table 4: Dimensions and test types of single crystal aragonite samples.

Sample Id	Gauge length (Round to Round) (inch)	Diameter (inch)	Mechanical test
1	0.136	0.095	Torsion
2	0.077	0.142	Tension

3.2 Mechanical Testing

3.2.1 Fixtures

Different types of fixtures were tested for mechanical testing including stainless steel fixture with rectangular holes, double clamping steel fixture, U-shaped clamps, independent four-jaw chuck and dependent four-jaw chuck. Results showed that the U-shape clamps (Figure 31a) are good for tension as they provide efficient contact to pull the sample apart. In addition, independent four-jaw chuck (Figure 31b) clamps are good for torsional tests as they provide effective contact under torsional loads.

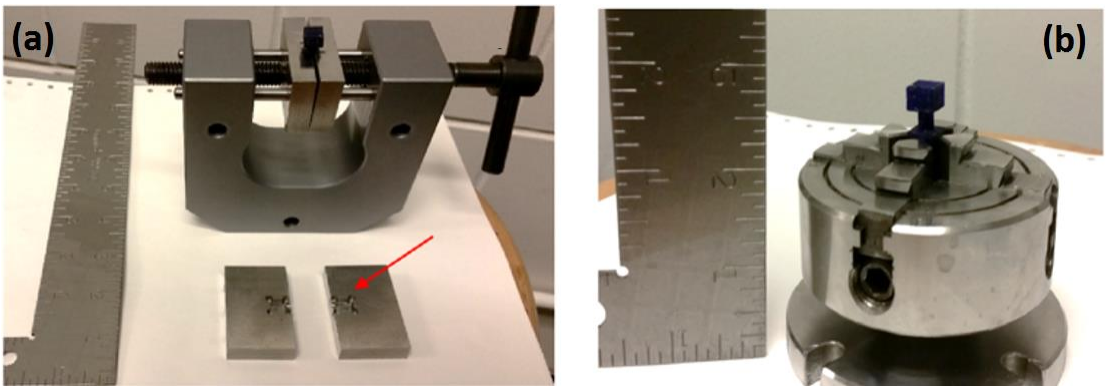

Figure 31: Photographs of the fixtures used for mechanical testing. (a) U-shaped clamps; and (b) independent four-jaw chuck clamps.

3.2.2 Mechanical Testing system

Both torsion and tension tests were performed using eXpert 8600 Series Axial-Torsion Testing Systems (ADMET, Norwood, MA).

Figure 32: A photograph of the ADMET testing system showing two load cells stacked on each other.

To detect small physical changes during mechanical tests, a dual system was developed to include two load cells and to collect data at a sampling rate of 200k per second and at the resolution of 22-bit simultaneously. This configuration promotes high precision measurements through two parallel data paths.

3.2.3 Mechanical Testing System

3.2.3.1 Dual Transducers

In the testing system, we employed two load cells to measure the sample response during monotonic torsional tests under displacement control. A small torque load cell with the capacity of 25 lb-in (Futek, Irvine, CA) is mounted on a an axial-torsion load cell that has an axial capacity of 1000 lbs and a torque capacity of 500 lb-in (ADMET, Norwood, MA). A similar setup was used for the tension tests. The only difference is that the 25 lb-in load cell was replaced by a 50 lb (Transducer Techniques, Temecula, CA) axial load cell. In addition, the load cells were excited by a 10 DCV using the PWS2185 DC power supply (Tektronix, Oregon, USA). Load cell specifications are provided in Table 5 below.

Table 5: A summary of load cells technical specifications.

Load cell	Manufacturer	Model	Capacity	Output
500lb-in (Axial/Torsional)	Admet	1216CEW-1K	500 lb-in torque 1000 lb axial	1.531 mV/V 2 mV/V
25 lb (Axial)	Futek	TFF400	25 lb-in	1.97 mV/V
50 lb (Axial)	Transducer Techniques	DSM-50	50 lb	2 mV/V

3.2.3.2 The Dual Data Acquisition System

While the data generated from the 500 lb-in is acquired using MtestQuatro's system (Admet, Norwood, MA); the data from the 25 lb-in load cell is obtained via two data acquisition devices. The first one is a 22-bit Agilent 34972A data acquisition, (Keysight Technologies, Santa Rosa, CA). The other one is 14-bit U2531A simultaneous data acquisition unit, (Keysight Technologies, Santa Rosa, CA). The sampling rate of the latter

can reach up to 2 million samples per second. A schematic of the dual data acquisition system is shown in Figure 33.

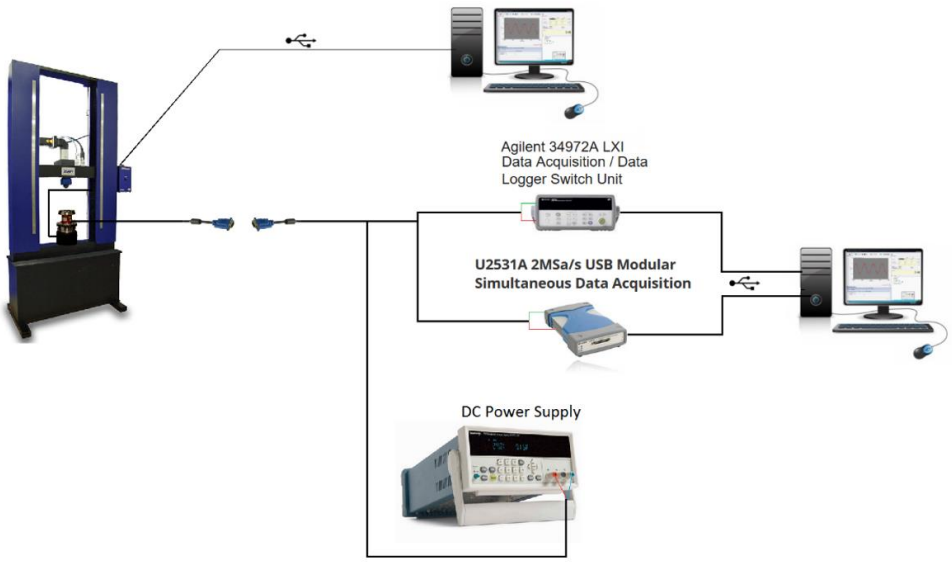

Figure 33: A schematic of the dual data acquisition system.

A comparison between the two data acquisition systems is shown in Table 6 below.

Table 6: Data acquisition devices resolutions and sampling rates.

	Agilent 34972A	Agilent U2531A
Resolution	22-bit	14-bit
Maximum sampling rate	27 samples/sec	2 million samples/sec

The 22-bit DAQ provides high resolution while the 14-bit DAQ provides high sampling rates. By using the dual system, data with high resolution and high sampling frequencies are collected at the same time. High sampling frequency data collection will

cover the full spectrum of signals and increase the signal to noise ratio (SNR). Further, high resolution data will provide the smallest measurements of the events during the tests, which are critical to elucidate the impact of microstructure on the crack propagations. The lowest torsional load that can be detected using the 25 lb-in load cell is ~ 6E-4 lb-in.

3.2.4 Load Cells Calibrations and Pseudo-Samples Tests

Calibrations were performed on all load cells using weights ranging from ~0.0022 to 16 lbs. In addition, tens of monotonic torsion and tension tests were performed using plastic and chalk samples before testing nacre samples. Calibration charts for the 14-bit DAQ and the 22-bit DAQ are shown in Figure 34 and Figure 35, respectively.

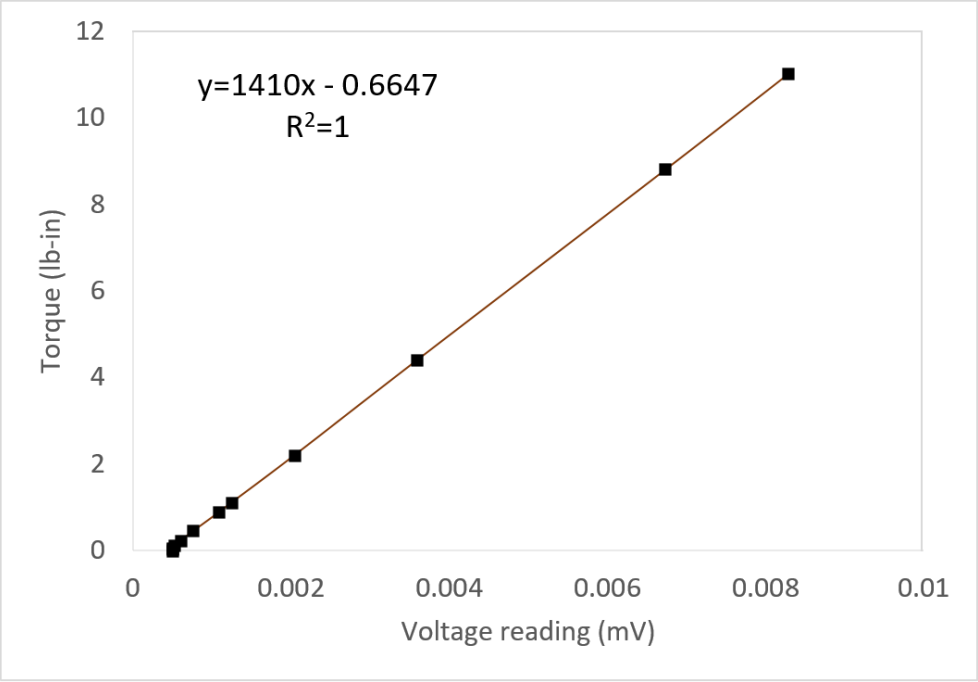

Figure 34: The calibration chart of the 14-bit DAQ with the 25 lb-in load cell.

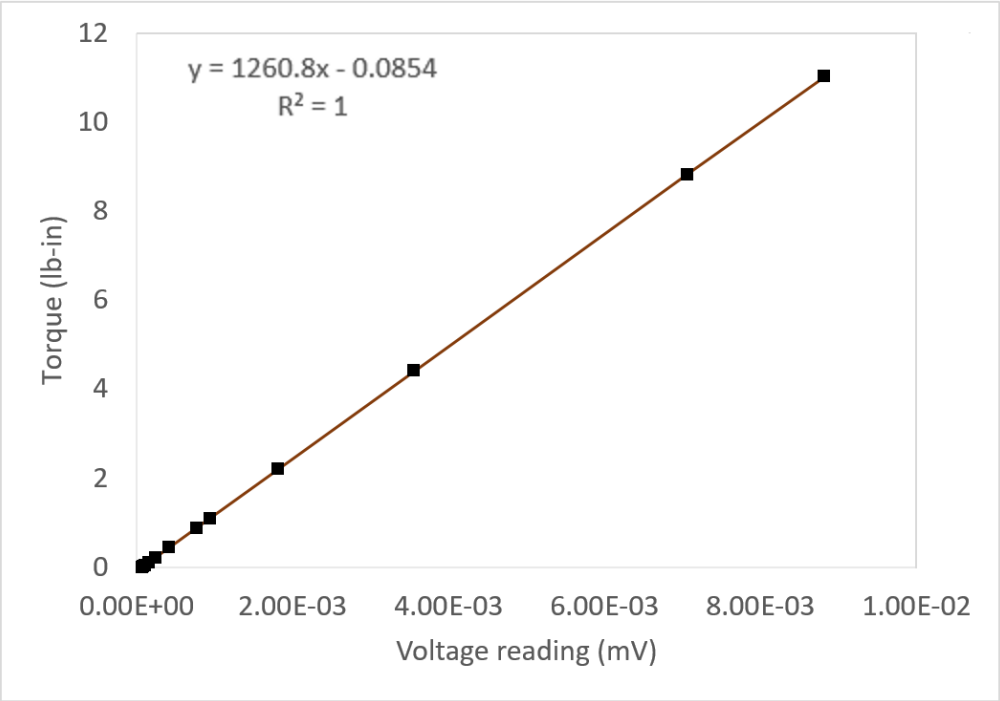

Figure 35: The calibration chart of the 22-bit DAQ with the 25 lb-in load cell.

3.2.5 Mechanical Tests

Mechanical tests were conducted to characterize the mechanical behavior of dog-bone shaped samples made from red abalone under pure shear and tensile stresses.

3.2.5.1 Monotonic Torsional Tests

Torsional tests were performed to study the interfacial shear resistance of nacre. Under torsional loads, pure shear stresses exist over the entire gauge section of the dog bone specimens. Monotonic torsional tests were conducted using eXpert 8600 Axial-Torsion testing systems, (ADMET, Norwood, MA). Displacement control was used to

apply the torque at the loading rate of 90 degrees/min. Testing information are summarized in Table 7 below.

Table 7: Parameters used in the dual data system to perform monotonic torsion tests.

Sample Id	Loading Rate (Degree/min)	Sampling rate (Sample/sec)			Torsional preload (lb-in)	Tensile Preload (lb)
		ADMET	22-bit DAQ	14-bit DAQ		
1	90	50	27	200000	0.3	0.05
9	90	50	27	200000	0.3	0.05
10	90	50	27	200000	0.3	0.05
Aragonite sample (A1)	90	50	27	200000	0.3	0.05

3.2.5.2 Monotonic Tension Tests

Tension tests were selected to apply normal loads over the entire cross section. Monotonic tension tests were conducted using the eXpert 8600 axial-torsion testing systems, (Admet,, Norwood, MA). Displacement control was used to apply the tension at 0.01 in/min loading rate. Testing information are summarized in Table 8.

Table 8: Parameters used in the dual data system to perform monotonic tension tests.

Sample Id	Loading Rate (Inch/min)	Sampling rate (Sample/sec)			Torsional preload (lb-in)	Tensile Preload (lb)
		ADMET	22-bit DAQ	14-bit DAQ		
5	0.01	50	27	200000	0	0
8	0.01	50	27	200000	0	0
Aragonite sample (A2)	0.01	50	27	200000	0	0

3.2.7 Test Data

Voltage readings from the small load cells were collected using 14-Bit and 22-Bit data acquisitions systems. The voltage readings were, then, converted to loads by using the calibration charts. The parameters used for each DAQ are summarized in Table 9 below:

Table 9: The parameters used for acquiring the data using the 14-bit and 22-bit data acquisition devices.

	22-bit DAQ	14-bit DAQ
Sampling frequency (samples/sec)	27	200000
Averaged	Yes	No
Polarity	Bipolar	Bipolar
Maximum input voltage (V)	±5	±10
Offset	0	0

The voltage readings gathered by the 14-bit DAQ using 200k samples per second were huge. For a torsion test lasting 10 minutes, the number of data points exceeds 120 million, resulting in a comma separated value (CSV) file that is around 10 Gigabytes. Therefore, both MATLAB software and open source Python programming language were used to process the data. A simple Python code was developed to load the CSV files and perform simple mathematical and statistical operations such as moving average, median and multiplication. MATLAB was also used to filter the data using a digital low pass filters (Shenoi, 2005). A low pass second-order Butterworth filter was finally selected to extract the essential curves. Representative filter curves are shown in Figure 36.

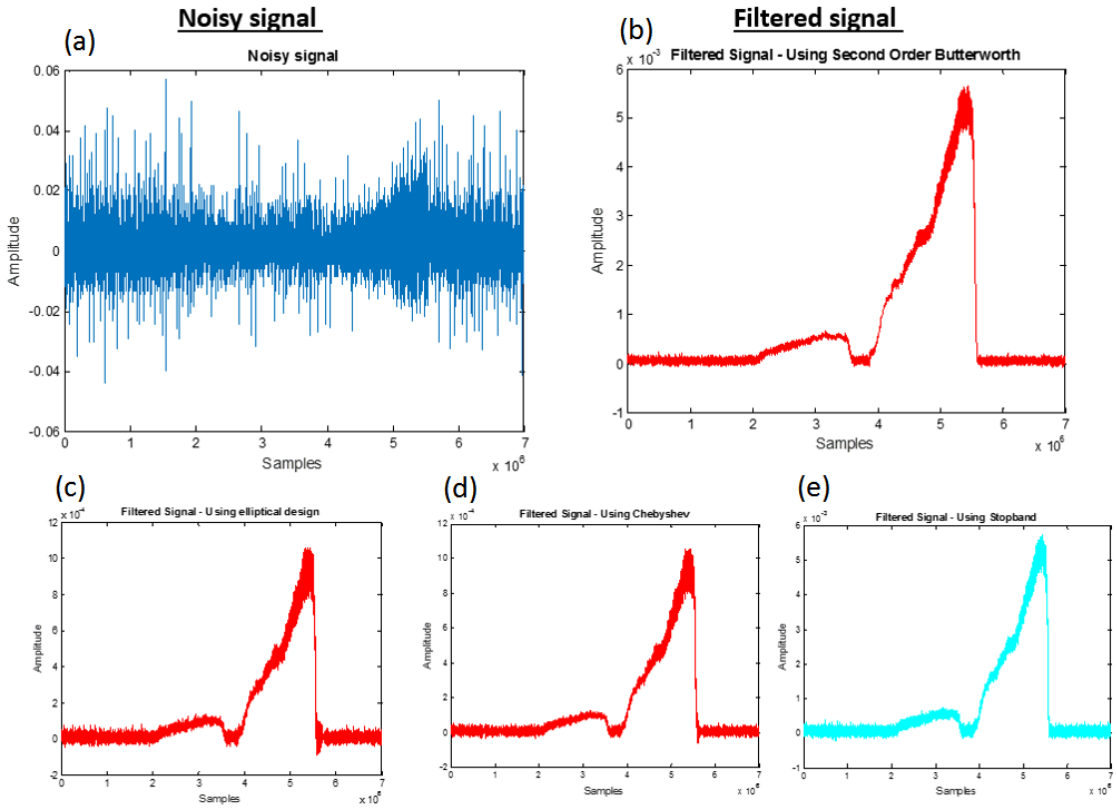

Figure 36: A comparison between the performance of three digital filters (a) the noisy signal; (b) the filtered signal using a second order Butterworth digital low pass filter; (c) the filtered signal using Elliptical digital filter; (d) the filtered signal using Chebyshev digital filter; and (d) the filtered signal using a second order Butterworth digital stop band digital filter.

3.3 Tensile and Shear Strength

3.3.1 Tensile Strength Calculations

The tensile strength was given by:

$$\sigma_f = \frac{F}{A}$$

Where *F* is the peak applied load, and *A* is the cross-sectional area of the nacreous gauge section of the samples

3.3.2 Shear Strength

The shear strength was given by:

$$\boldsymbol{\tau_{max}} = \frac{\mathbf{Tc}}{\mathbf{J}}$$

Where τ_{max} is the maximum shear stress on the circumference of the cylinder, *T* is peak torque, *c* is the radius of the gauge section, and *J* is the polar moment of inertia.

3.4 Microscopic Characterization

Two microscopes were used to characterize the fracture surfaces of the failed samples;

3.4.1 Optical Imaging

The fracture surfaces of the failed specimen were examined using digital optical microscope (Aven, Ann Arbor, MI). This microscope provides colored images in low magnification.

3.4.2 Scanning Electron Microscopy

The fractured surfaces of the samples were sputter-coated with gold/palladium for SEM imaging. The coated samples were then examined using JEOL 6060 Scanning

Electron Microscope (JEOL USA, Peabody, MA). The voltages of the electron beams ranged from 5 to 25 kV.

3.5 Finite Element Models

When a sample breaks under torsion, the shear stress distributions are identical in the circumference of the gauge section. Hence, shearing occurred between two adjacent nacreous tablets around the perimeter at the same time. Finite element models were established to investigate the mechanical responses under shearing between two tablets. The materials used in the models were assumed linear elastic. This assumption was based on the torque-angle measurements that show linear elastic response with a correlation coefficient (R^2) very close to 1 (Figure 42). Interfaces between the two tablets are 30 nm thick containing shear pillars, asperities and organic matrices (5% of the tablet area). The tablets were modeled as hexagons with 3-μm length and 0.5-μm thickness. Young's modulus of tablets was 100 GPa. Pillars and asperities were 50 nm in diameters. Pillars were modeled as circular columns connecting the two tablets. Asperities, however, were modeled as half spheres with height of 15.5 nm. In this configuration, only a small portion of asperity surfaces was in contact with the other asperities. Once two asperities contact each other, they do not contact other asperities. The overlap area between the two tablets was chosen to be 1/3 of a table surface (Barthelat et al 2007). The finite element study was performed using a synergy of ABAQUS™, Python scripts and MATLAB software. The synergy is schematically illustrated in Figure 37. A representative model of adjacent tablets is shown in Figure 38.

Figure 37: A schematic showing software involved in the finite element study.

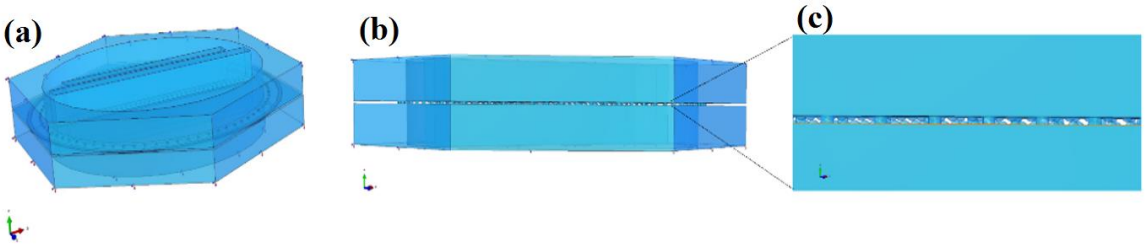

Figure 38: The finite element model (a) A three-dimensional view of the model; (b) A side view of the model; (c) A closer look at interface between the two tablets.

3.5.1 Objectives of the Finite Elements Study

The objective of this mathematical study is to quantify the contribution of individual toughening mechanisms to the interfacial shear resistance of nacreous structures, including shear pillars, nano-asperitites and protein chains.

3.5.2 Models Features

Table 10: Parameters studied in the finite element models.

Parameter	Range
Number of shear pillars	1 to 750
Number of nano-asperities	1 to 807
Shear pillars' Young's modulus	0.1, 40 and 100 GPa
Nano-asperities' Young's modulus	0.1, 1.6 and 100 GPa
Organic matrix' Young's modulus	20 MPa, 1 GPa and 20 GPa
Compressive load	0, 1kPa, 100 kPa

3.5.3 Boundary Conditions

The model consisted of two tablets stacked on each other as shown in Figure 38. Encastre boundary condition was applied to the bottom surface of the lower tablet. The upper tablet was fixed on its top surface in all directions except the horizontal displacement and the vertical pressure directions. A normal frictionless contact interaction was assigned to asperity surfaces. In addition, a displacement of ~10 nanometer was assigned to the representative node on the top tablet. This value was based on the measured rotations, which included the rotations of transitional sections of the dog specimens and of the 25 lb-in load cell. More effort is needed to quantify this displacement to accurately provide model inputs.

3.5.4 Meshes

The model was meshed using linear, tetrahedron elements. Finer mesh elements were assigned to the asperities, pillars and organic matrix's and regions around them. Each model consisted of approximately 200,000 to 300,000 elements.

EXPERIMENTAL RESULTS

4.1 Torsion Tests Results

In monotonic torsional tests, torque-rotation curves were collected to document the specimen failures. Each curve is separated into two segments; an increment region and a sudden drop indicating a catastrophic failure. Torque-rotation curves are shown in Figure 39-42 below. The increment stages are straight paths fitted excellently using linear regressions. These curves indicated that nacreous interfaces exhibited primarily linear elastic responses prior to shear failure. All curves dropped to zero after peak loads. meaning that samples failed immediately when the interfacial shear strength was reached. All samples show helical stair fracture surfaces that are almost 45 degrees to the cylindrical axis. Consistent torque-angle curves were obtained between different samples, through which the average shear strength was ~33.5 MPa. Further, an aragonite sample failed via monotonic torsion (Figure 43) exhibited a shear strength of 13.2 MPa, which is less than the shear strength of nacre albeit being composed of aragonite. This decrease in shear

strength is an evidence that microstructures are critical in resisting cracks for polymorphic aragonite structures.

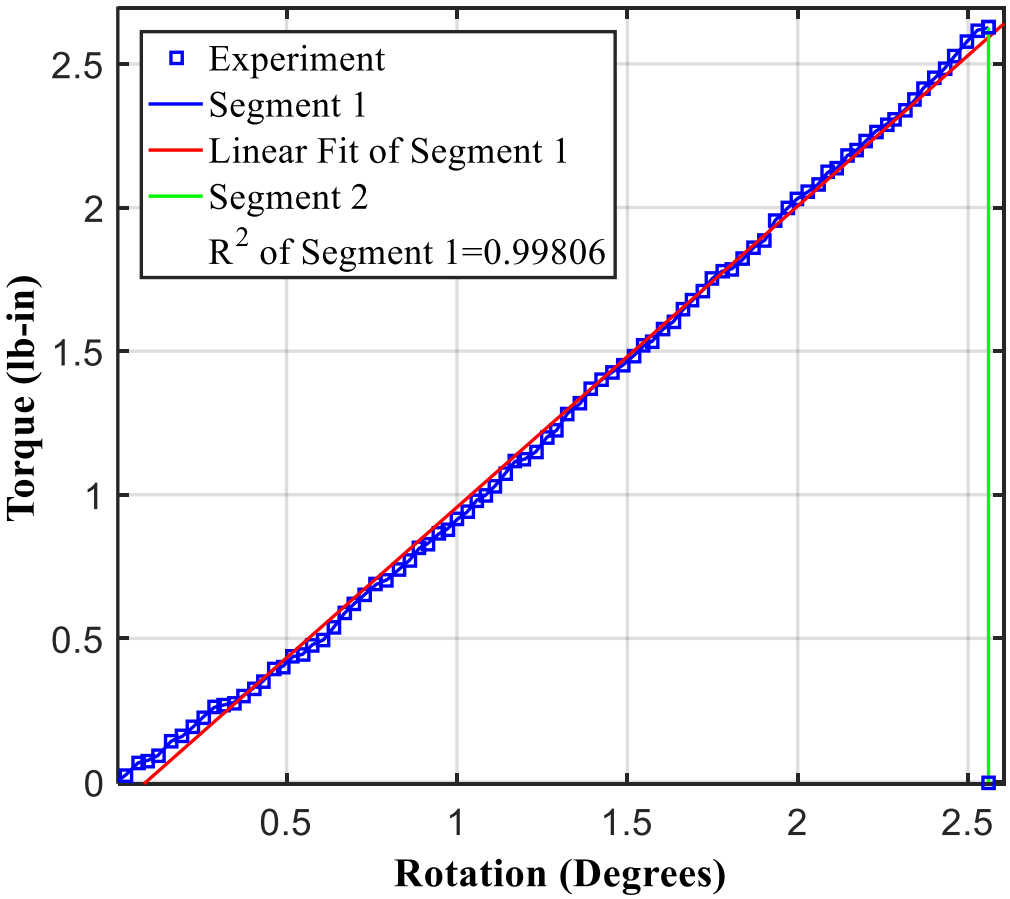

Figure 39: The torque-angle curve for nacre sample N1.

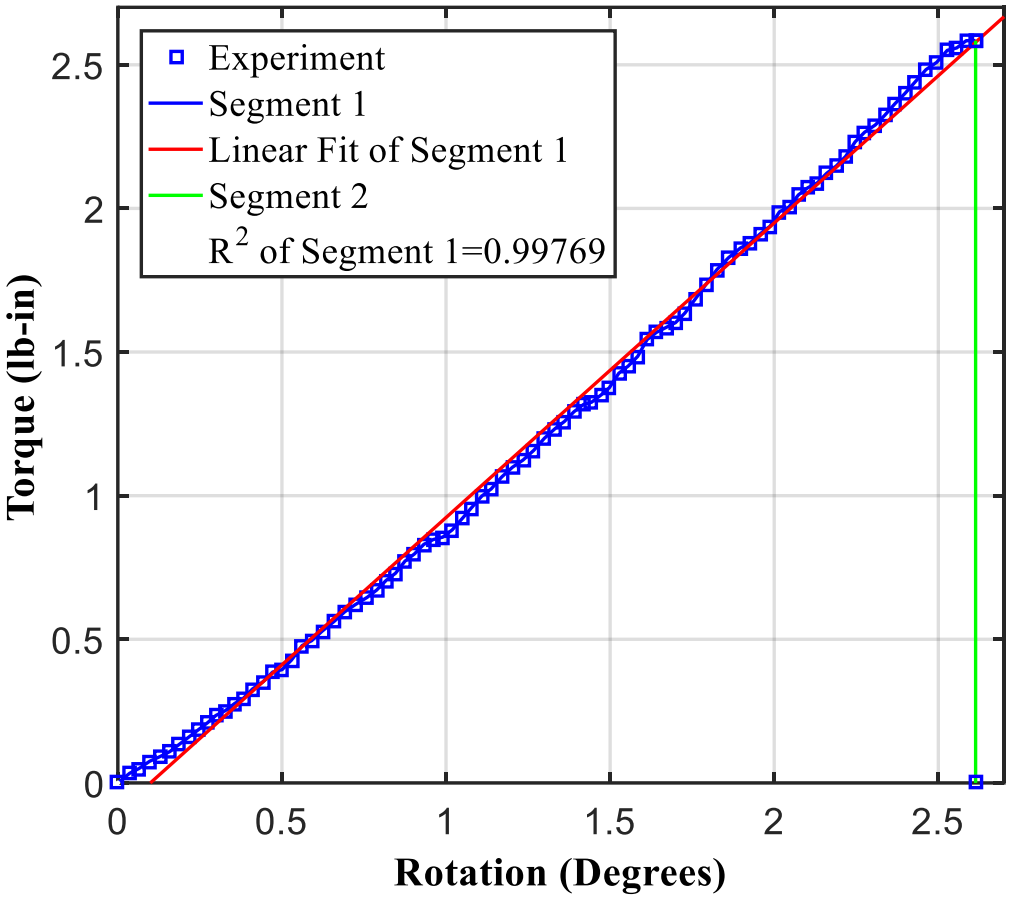

Figure 40: The torque-angle curve for nacre sample N9

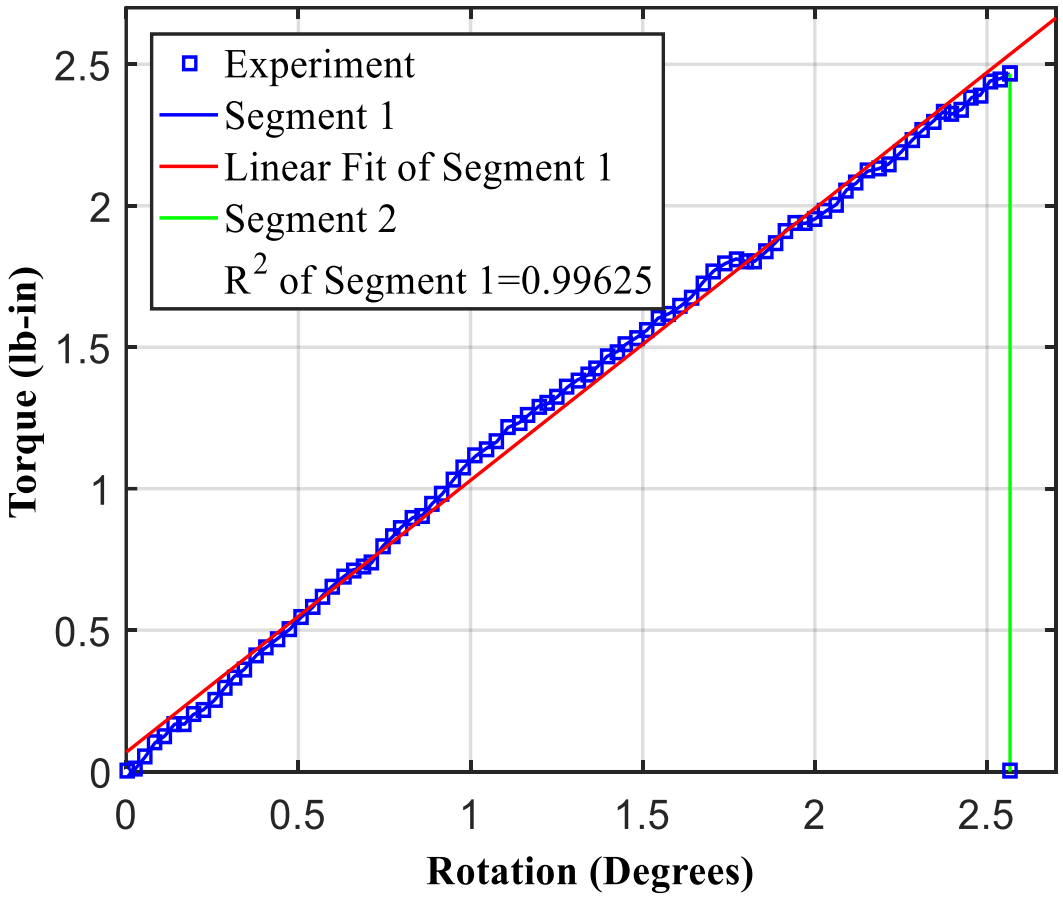

Figure 41: The torque-angle curve for nacre sample N10.

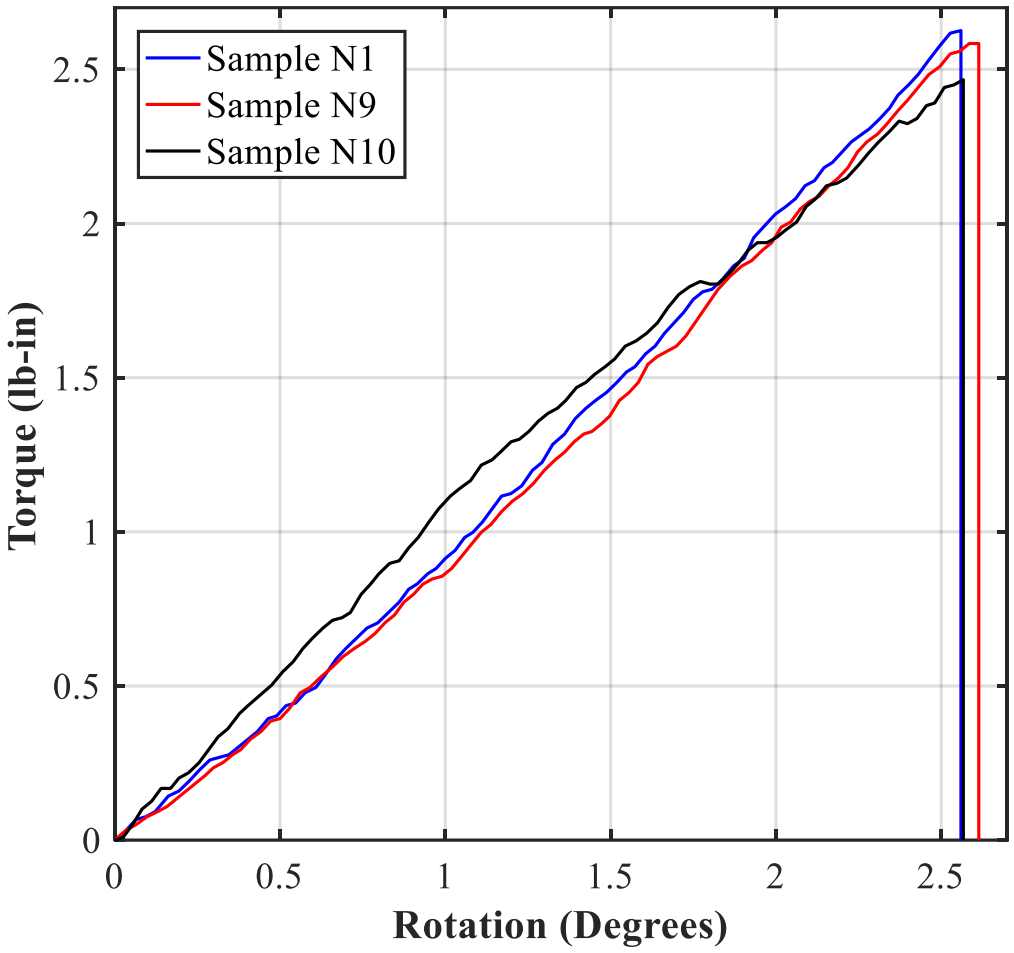

Figure 42: Overlaps of torque-angle curves.

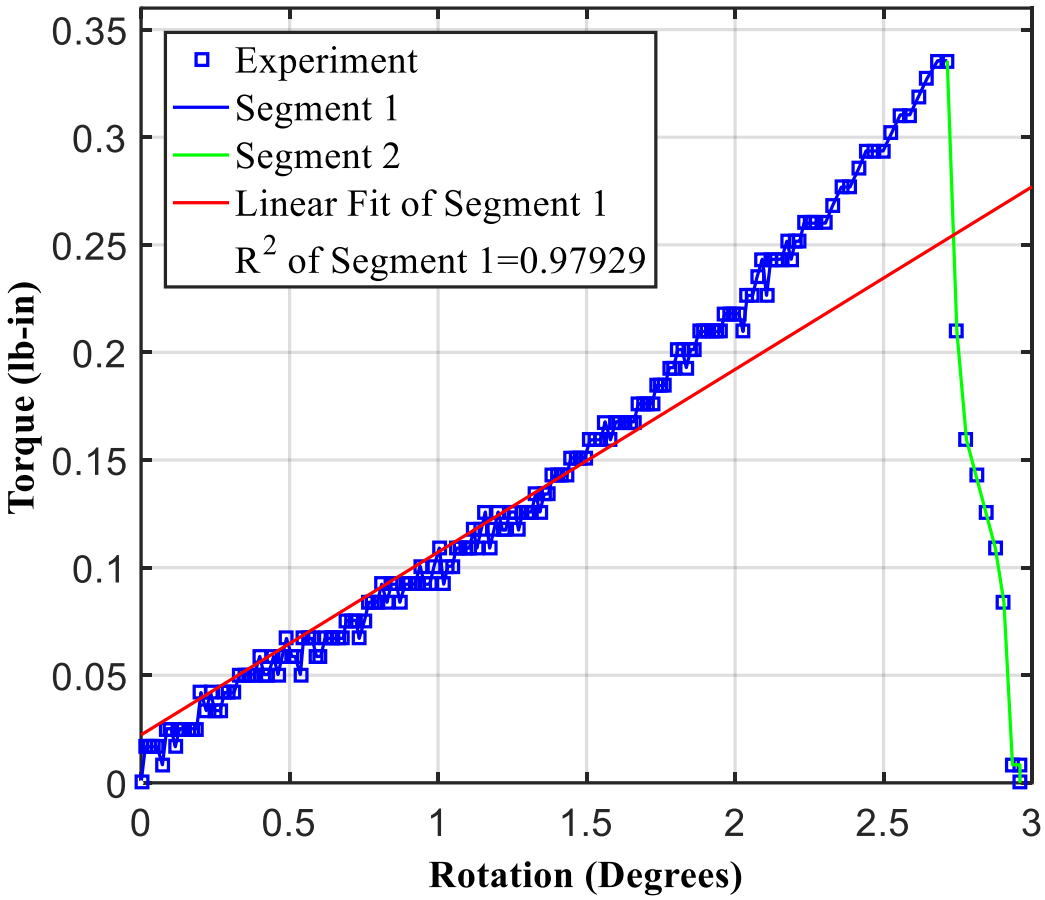

Figure 43: The torque-angle curve for aragonite sample A1.

4.2 Tension Tests Results

In monotonic tension tests, force-displacement curves were collected to show the mechanical responses. Each curve is separated into two segments: an increment region and then a sudden drop indicating a catastrophic failure. In the increment stages, curves showed small saw-tooth characteristics (Figure 46). This was probably due to the unsteady failure of the green matrices in the growth layers. As the tensile stresses increase, matrices

delaminate from column and spherulitic structures or split inside. The average tensile strength is ~2.1 MPa.

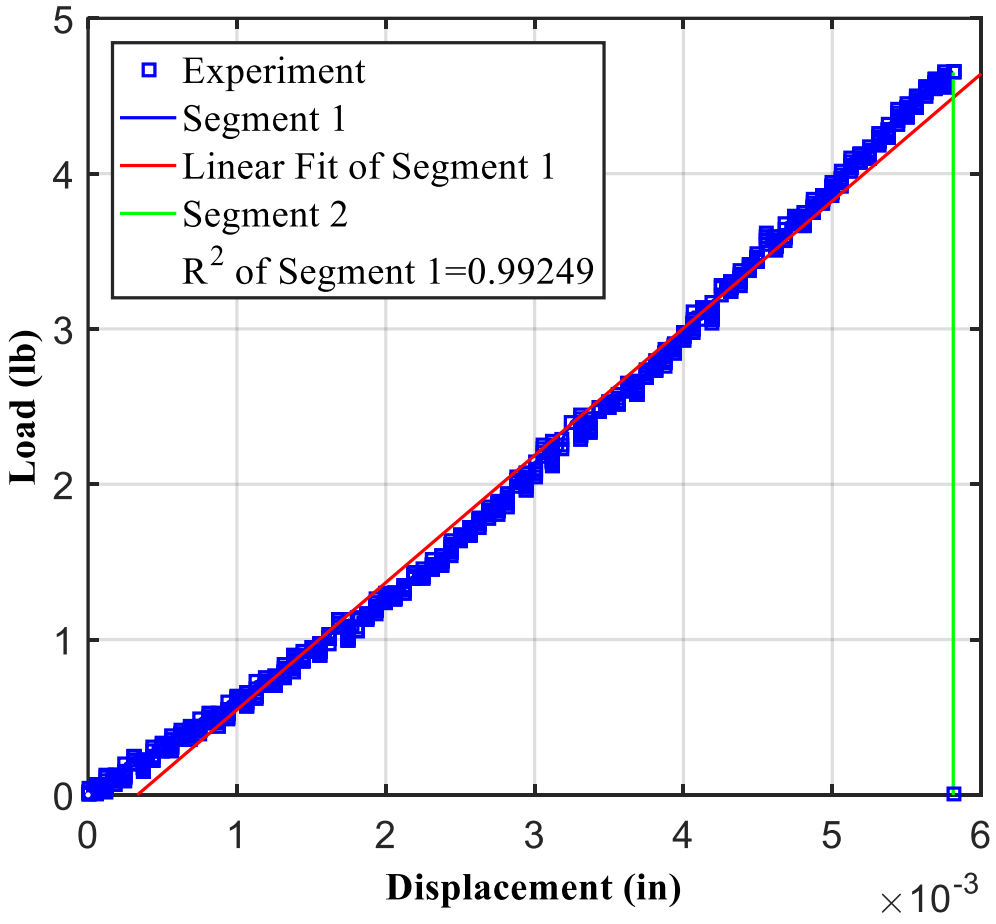

Figure 44: The load-displacement curve for nacre sample N5.

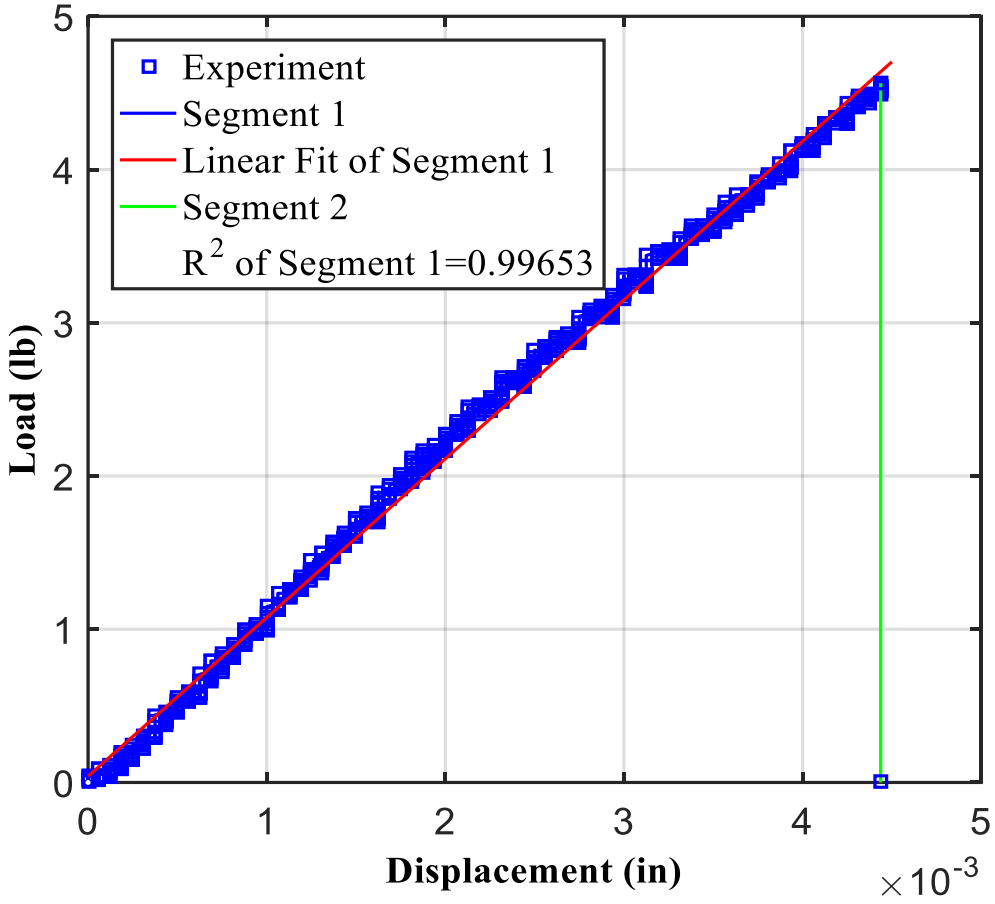

Figure 45: The load-displacement curve for nacre sample N8.

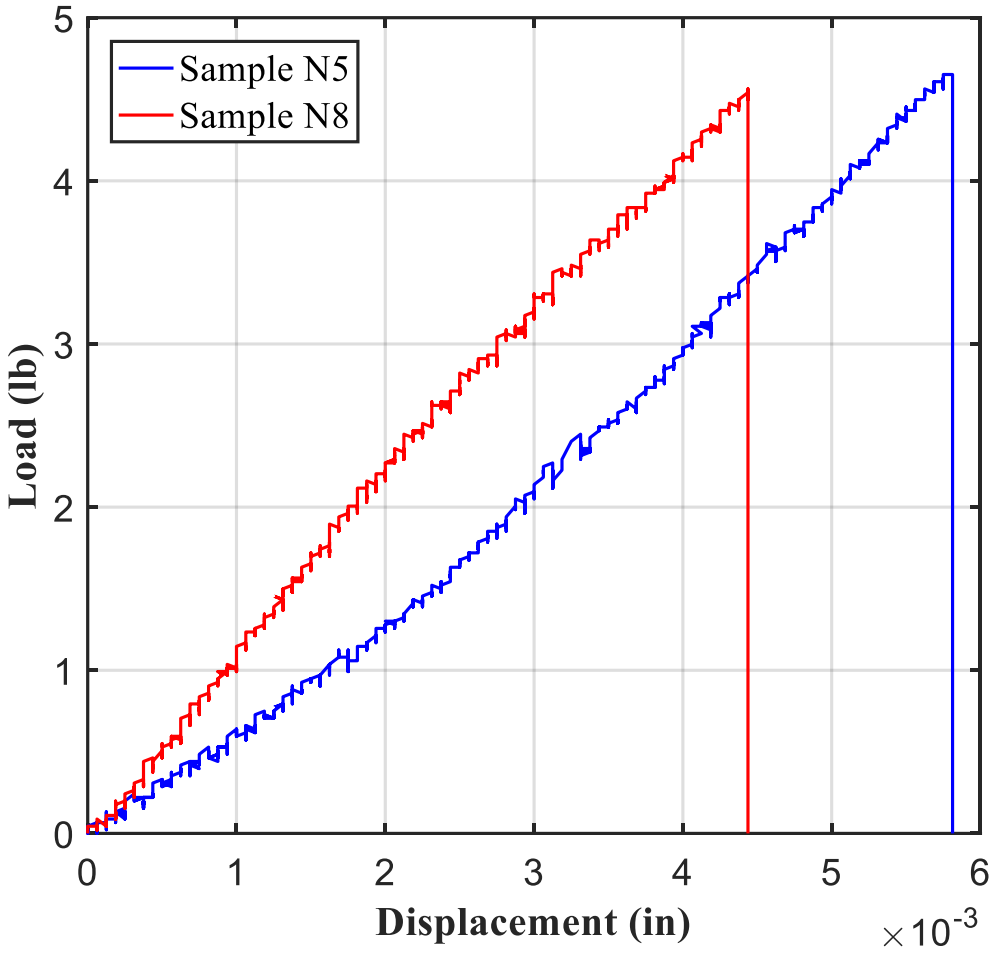

Figure 46: Overlaps of load-displacement curves.

FRACTOGRAPHIC CHARACTERIZATION

5.1 Torsional Specimens

Under torsion, all specimens fractured in the gauge sections. The fracture surfaces of these broken specimens are characterized using both optical and scanning electron microscopes. In general, the fracture surfaces of the failed specimens are approximately 45 degrees with respect to the cylindrical axis. When interfacial strengths were reached, cracks initiated from nacre and growth layers, and then propagated through the gauge section to fail the sample (Figure 47a). However, crack kinked between the growth layers and the surrounding nacreous structures, indicating that the shear resistance of nacre and growth layers are not the same (Figure 47b).

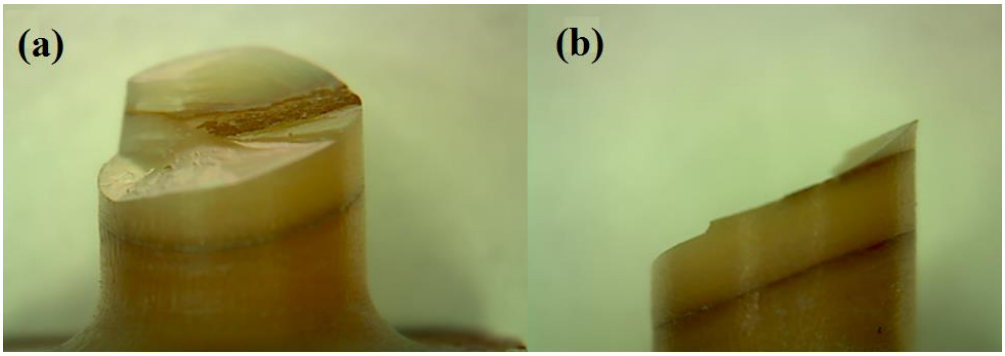

Figure 47: Images showing the helical fracture surface of a nacre sample failed under torsion (a) elevation view; and (b) side view.

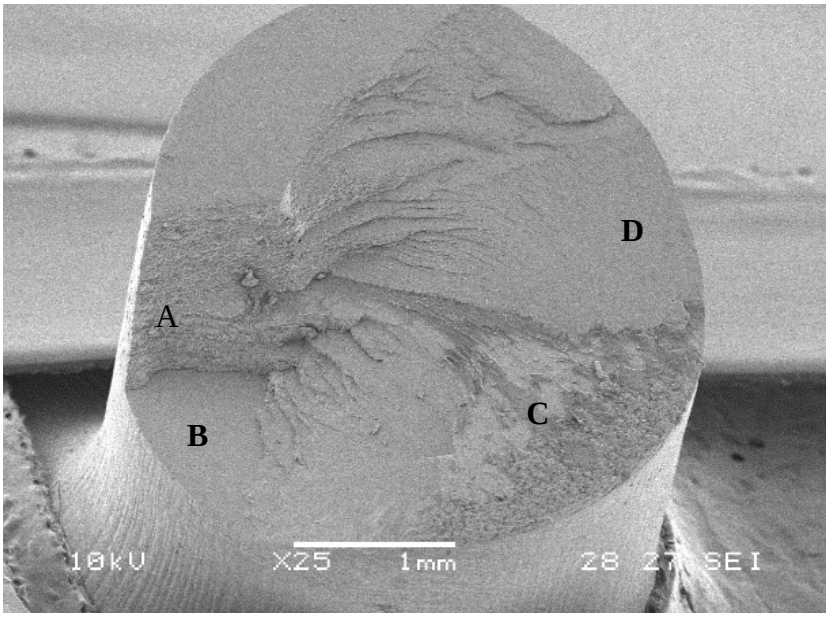

Figure 48: An SEM image showing the helical fracture surface of a nacre sample failed under torsion, (A): nacreous waterfall area consisting of a thin band of growth layer; (B): nacreous flat plane; (C): a growth layer, the helical nature of the fracture exposed different strata of the growth layer; and (D): nacreous layered helical section.

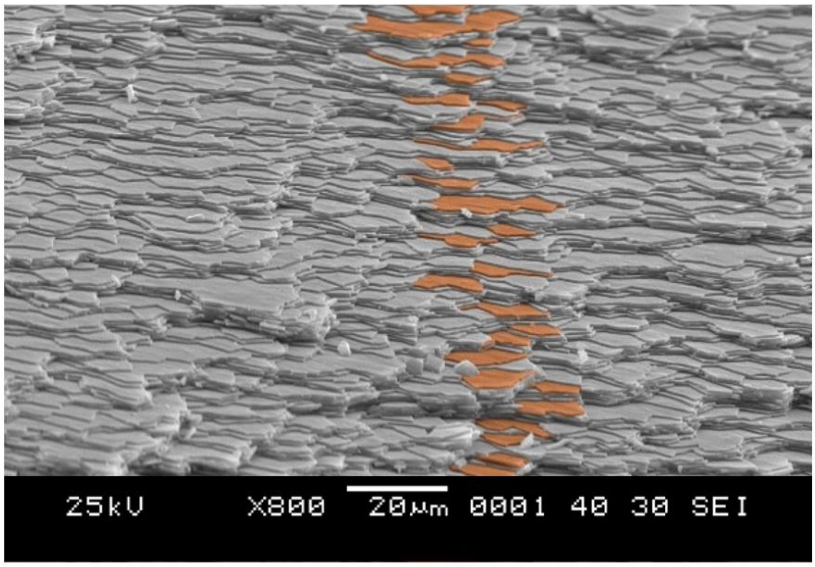

Figure 49: An SEM image showing the nacreous stairs in a sample failed under torsion.

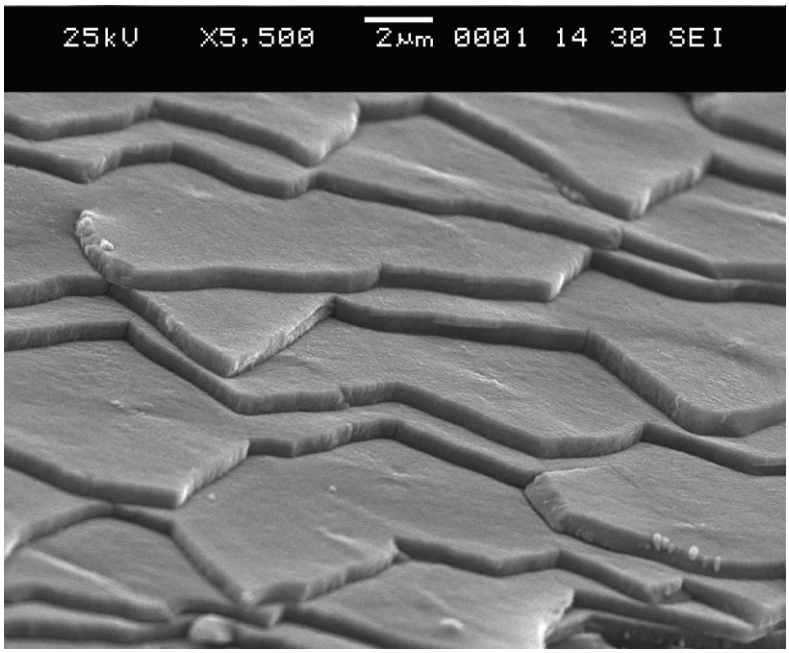

Figure 50: A closer look at the nacreous stairs (Hale-Sills, 2015).

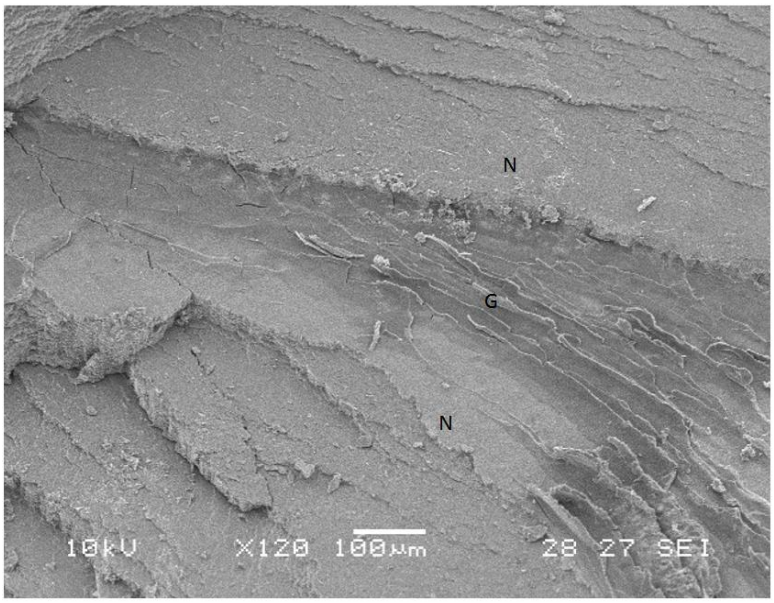

Figure 51: An SEM image showing the layers of the growth layer from the top, (N) nacreous structures, and (G) growth layer exposing its different strata.

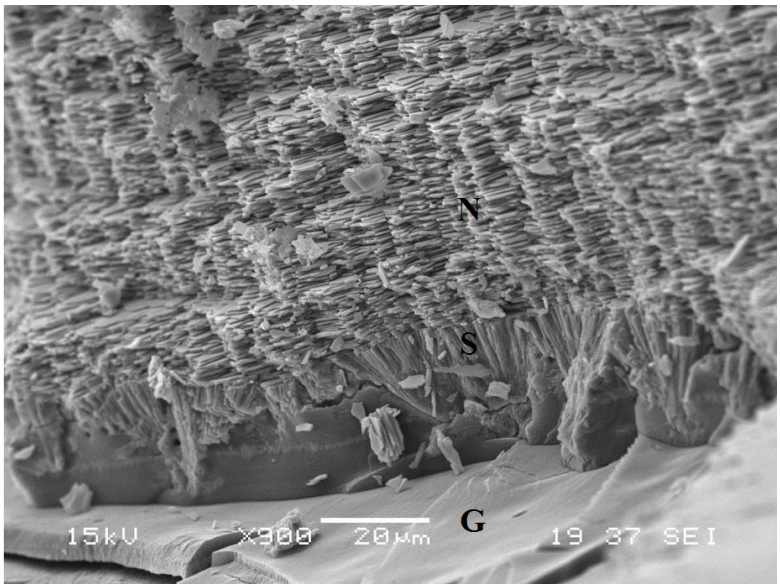

Figure 52: A view of the growth layer showing (G) green matrix, (S) spherulites and (N) nacreous structures.

5.2 Tension Specimens

In tension tests, all specimens fractured generally in the gauge section. The fracture surfaces of these broken specimens were characterized using both optical and scanning electron microscopes. In general, fracture surfaces of the failed specimens are perpendicular to the cylindrical axis, and occur within the growth layers with the minimal presence of nacreous structures.

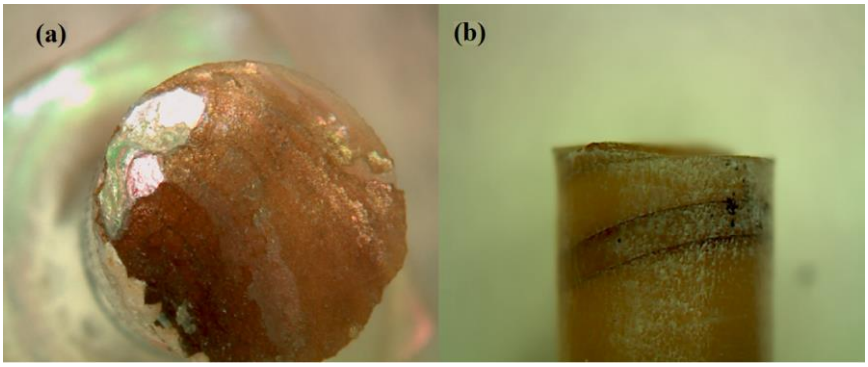

Figure 53: Images showing the flat fracture surface of sample failed under tension; (a) the top view of the fracture surface, barley showing any nacreous structure; (b) the side view.

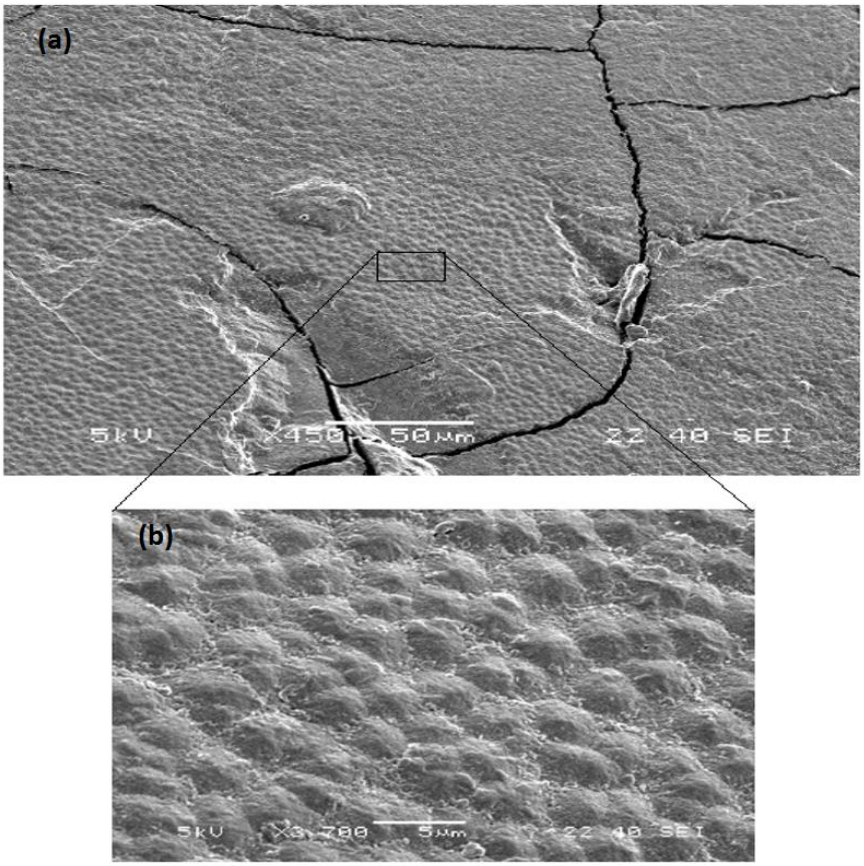

Figure 54: SEM images showing (a) the exposed spherulites in growth layer from the top; and (b) a close look at the bumpy nature of intact spherulites.

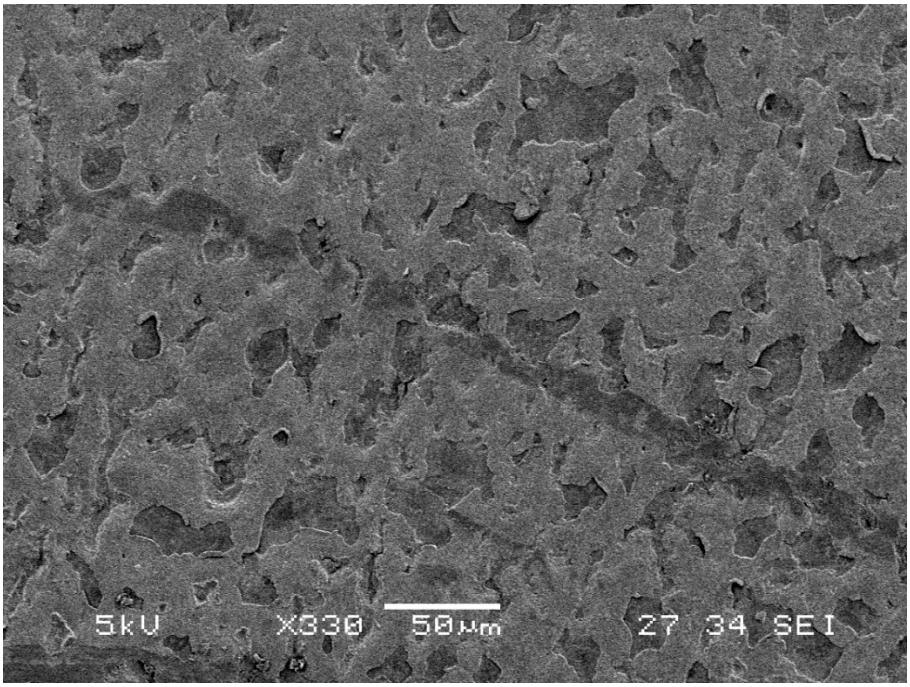

Figure 55: An SEM image showing the delaminated green matrices on the fracture surfaces of a sample failed under tension.

5.3 Preliminary Conceptual Models

The fractographic characterization showed that, under torsion, cracks initiate at the outer edge of the gauge section, and then propagate through both nacreous structures and growth layers. More efforts are needed to disclose which structures failed first. Under tension, however, crack initiate at growth layers, and then propagate through the growth layers. Unlike torsion sample, fracture surfaces from tension samples showed minimal presence of nacreous structure. These observations led to two preliminary conceptual models; First, both nacreous and growth layers structures fail under pure shear stresses (Figure 56). Second, growth layers are more susceptible to fracture under tensile stresses than nacreous structures, indicating that tablets interactions in nacre provide higher tensile

resistance than the green matrices that bonds spherulites and columns in the growth layers (Figure 57).

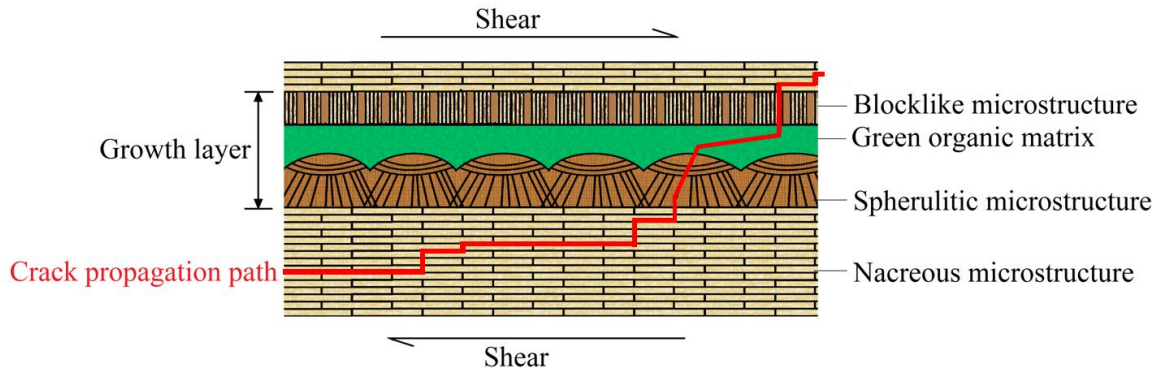

Figure 56: A schematic showing the crack paths in the polymorphic aragonite structures of red abalone under pure shear.

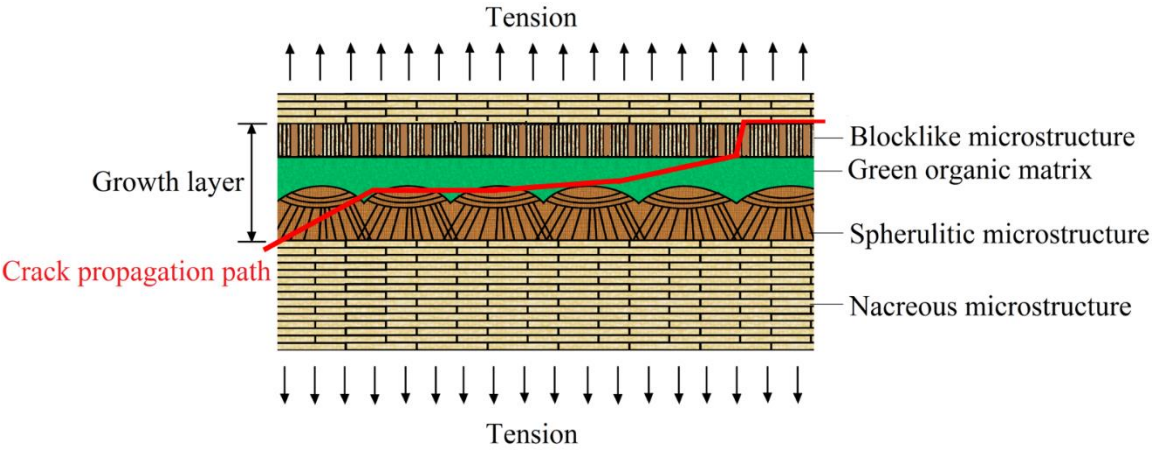

Figure 57: A schematic showing the crack paths in the polymorphic aragonite structures of red abalone under pure tension.

FINITE ELEMENT MODEL RESULTS

The objective of the finite element study was to use the iterative parametric study to quantify the contribution of individual toughening mechanisms based on asperities numbers, shear pillar numbers and material properties. A computational scheme is shown in Figure 58. In addition, pressure levels on the top tablet were also applied. The optimum

solution is achieved when the shear strength reaches 33.5 MPa, an approximation of the interfacial shear strength of nacre measured experimentally in prior sections.

Table 11: The material properties combinations used in the parametric finite elements study.

Combination	Asperities Young's modulus (GPa)	Shear Pillars Young's modulus (GPa)	Organic matrix Young's modulus (GPa)
1	0.1	0.1	0.02
2	1.6	0.1	0.02
3	100	0.1	0.02
4	0.1	40	0.02
5	1.6	40	0.02
6	100	40	0.02
7	0.1	100	0.02
8	1.6	100	0.02
9	100	100	0.02
10	0.1	0.1	1
11	1.6	0.1	1
12	100	0.1	1
13	0.1	40	1
14	1.6	40	1
15	100	40	1
16	0.1	100	1
17	1.6	100	1
18	100	100	1
19	0.1	0.1	20
20	1.6	0.1	20
21	100	0.1	20
22	0.1	40	20
23	1.6	40	20
24	100	40	20
25	0.1	100	20
26	1.6	100	20
27	100	100	20

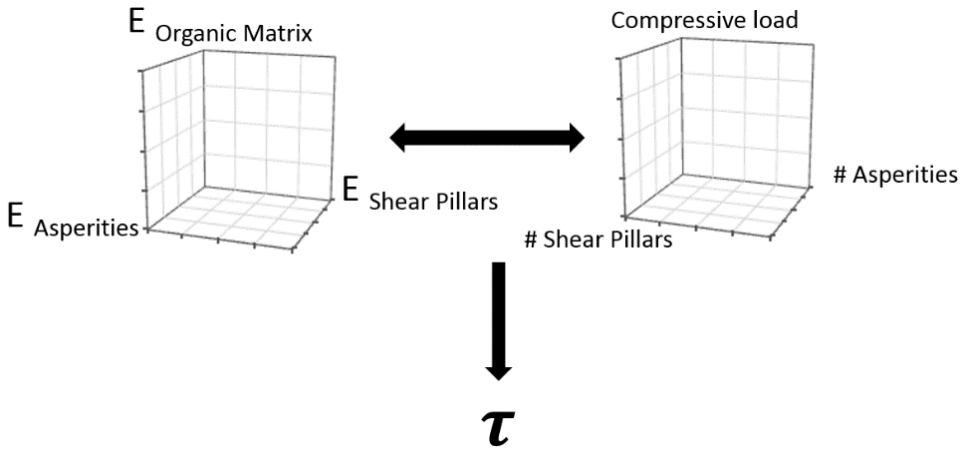

Figure 58: A schematic showing the iterative parametric process to quantify the contribution of individual toughening mechanisms based on asperities numbers, shear pillars numbers, material properties and pressure levels.

After iterations, upper and lower bounds of shear resistance were obtained, which are summarized in Table 12 and graphically presented in Figure 59.

Table 12: Parameters used in the FEM model to obtain interfacial shear strength comparable to experimental measurements.

Combination Number	Number of Asperities	Number of Shear pillars	Compressive load (kPa)	Shear stress (MPa)
9	19	8	0	29.108
9	24	8	0	36.768

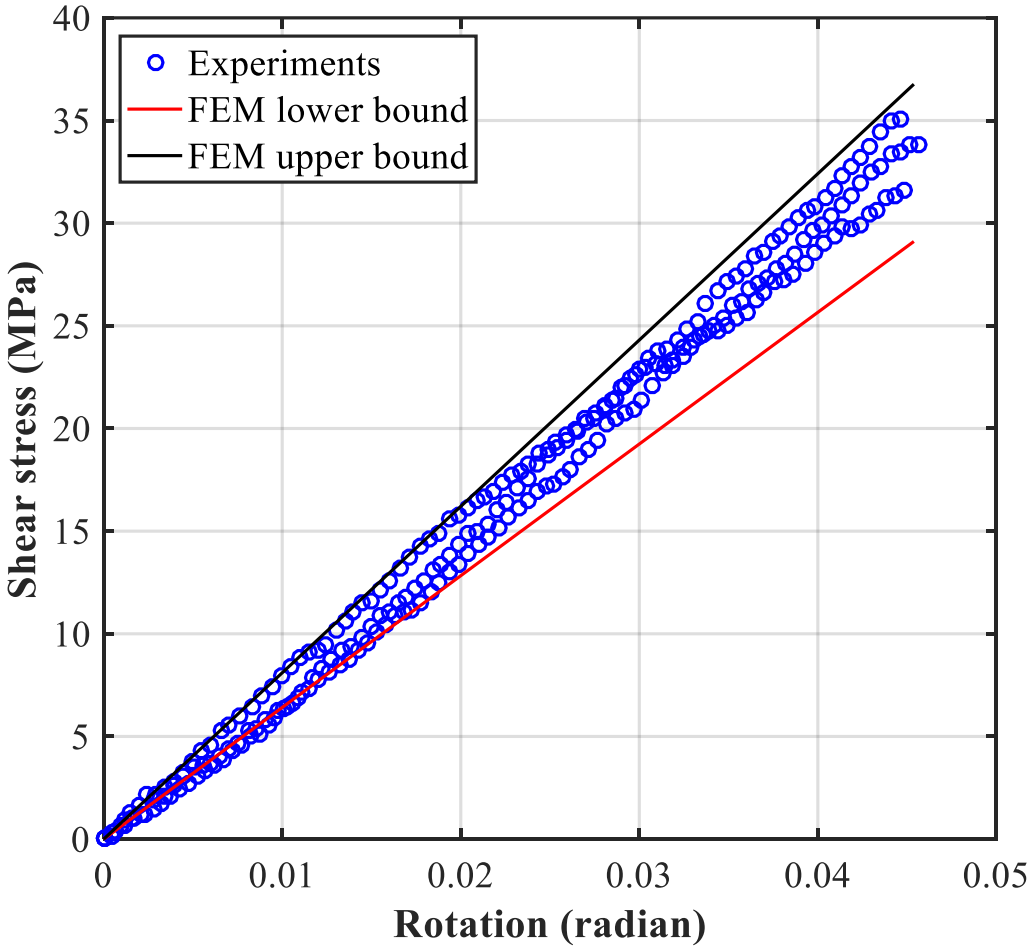

Figure 59: Comparison between the finite element predictions and experimental results**.**

To quantify each toughening mechanism's contribution to the interfacial shear strength of nacre, each toughening mechanism is analyzed in individual models. Stress contours of asperities and shear pillars are shown in Figure 60 and 61, respectively. Distributions of each mechanism to the shear resistance is illustrated in Figure 62.

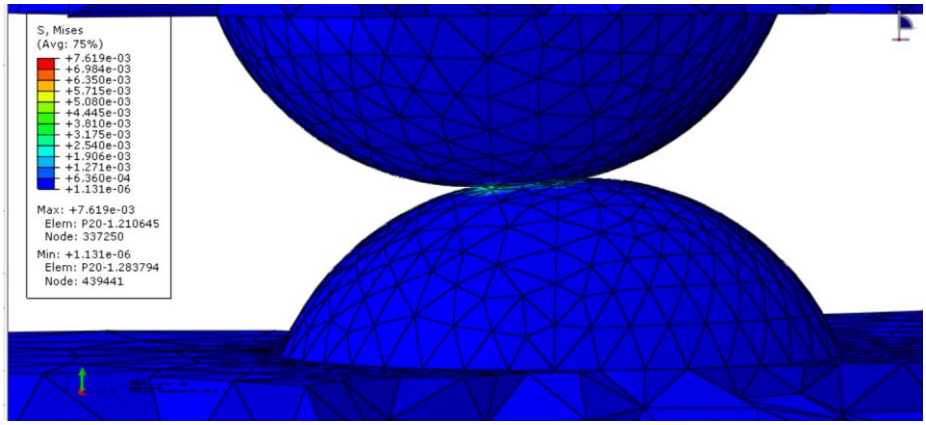

Figure 60: A screenshot of the finite element model showing the Mises stress contours on two asperities in contact.

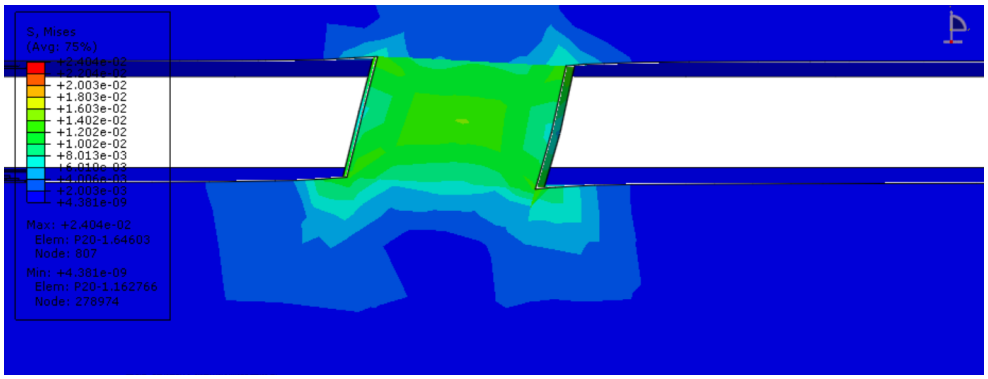

Figure 61: A screenshot of the finite element model showing Mises stress contours on a shear pillar being sheared.

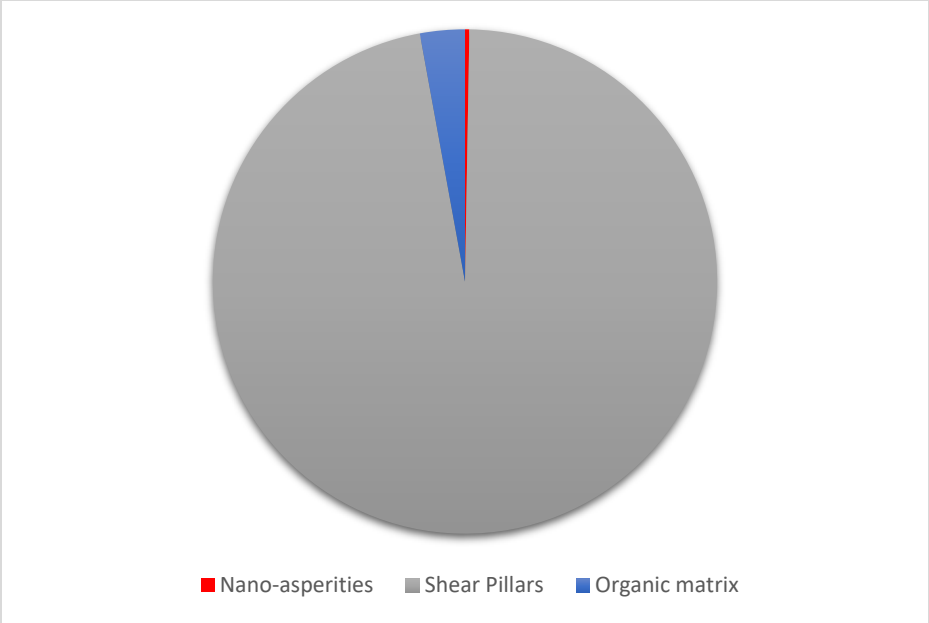

Figure 62: A pie chart showing the contribution of different toughening mechanisms to the interfacial shear strength of nacreous structures.

CONCLUSIONS

Despite being composed of weak calcium carbonate, nacre exhibits excellent mechanical properties due to its unique microstructure, which has been the focus of substantial research over the past few decades. However, limited research exists to quantify the contribution of individual toughening mechanisms (asperities, shear pillars and protein chains) to the interfacial shear strength of nacre, or to elucidate the failure mechanisms of the polymorphic structures in red abalone. In this study, an integrated experimental and numerical approach was used to study the interfacial strength of the polymorphic aragonite structures in red abalone.

First, a dual-data system was developed to collect both high frequency (200k samples/second) and high resolution (22-bit) data, in which the sample failure under pure tensile and shear stresses were quantified in detail. Second, dog-bone specimens containing growth layers and nacreous structures from red abalone shells were successfully created. Third, the mechanical responses of the polymorphic aragonite structures were measured using monotonic torsion and tension tests. Results showed that the interfacial shear strength of red abalone was ~33.5 MPa; while the tensile strength of polymorphic aragonite structures was ~2.1 MPa. By comparing the shear strength of red abalone to the shear strength of aragonite minerals, i.e., ~13.23 MPa, it was shown that microstructures were essential to the interfacial shear resistance of polymorphic aragonite structures. Torque-rotation curves under pure shear of polymorphic aragonite structures exhibited almost linear incrementing segments followed by sharp dropping segments. However, force-

displacement curves from tension tests exhibited saw-tooth characteristics in the incremental stages.

Fourth, fractographic characterization was conducted using optical and scanning electron microscopes. Samples failed under torsion exhibited helical fracture surfaces oriented at 45 degrees to the cylindrical axis, in which exposed nacreous stairs and growth layers were observed. Cracks initiated through both nacreous structures and growth layers, and propagated through the gauge section to fail the specimens. However, in tension tests, samples failed within the growth lines showing minimal presence of the nacreous structures. These characterizations showed that growth layers are more susceptible to fracture under tensile stresses. More efforts are needed to quantify the shear resistance of nacre and growth layers.

Fifth, finite elements models were developed to quantify contributions of shear pillars, asperities and protein chains to the interfacial shear resistance of nacreous structures. Results showed that shear pillars are dominant in resisting shear which is consistent with results in literature. The findings of this study can extend our understanding of the mechanics of natural materials and promote the research and development of high performance bioinspired materials.

REFERENCES

Aragonite mineral information and data: Aragonite. Retrieved July 3, 2016, from http://www.mindat.org/min-307.html

Barthelat, F. and Espinosa, H. D. (2007). An experimental investigation of deformation and fracture of nacre–mother of pearl. *Experimental mechanics*, *47*(3), 311-324.

Barthelat, F., Li, C. M., Comi, C. and Espinosa, H. D. (2006). Mechanical properties of nacre constituents and their impact on mechanical performance. *Journal of Materials Research*, *21*(08), 1977-1986.

Barthelat, F., Tang, H., Zavattieri, P. D., Li, C. M. and Espinosa, H. D. (2007). On the mechanics of mother-of-pearl: a key feature in the material hierarchical structure. *Journal of the Mechanics and Physics of Solids*, *55*(2), 306-337.

Bass, J. D. (1995). Elasticity of minerals, glasses, and melts. *Mineral physics & crystallography: a handbook of physical constants*, 45-63.

Bertoldi, K., Bigoni, D. and Drugan, W. J. (2008). Nacre: an orthotropic and bimodular elastic material. *Composites Science and Technology*, *68*(6), 1363-1375.

Callister, W. D. (2007). *Materials science and engineering: An introduction*. New York: John Wiley & Sons.

Checa, A. G., Cartwright, J. H. and Willinger, M. G. (2011). Mineral bridges in nacre. *Journal of structural biology*, *176*(3), 330-339.

Currey, J. D. (1977). Mechanical properties of mother of pearl in tension. *Proceedings of the Royal Society of London B: Biological Sciences*, *196*(1125), 443-463.

Dashkovskiy, S., Suhr, B., Tushtev, K. and Grathwohl, G. (2007). Nacre properties in the elastic range: Influence of matrix incompressibility. *Computational Materials Science*, *41*(1), 96-106.

DATAQ Instruments, Inc. (n.d.). Data Acquisition (DAQ). Retrieved September 13, 2016, from http://www.dataq.com/data-acquisition/

Davis, J. R. (2004). *Tensile testing*. Materials Park, OH: ASM International.

Dunlop, J. W. and Fratzl, P. (2010). Biological composites. *Annual Review of Materials Research*, *40*, 1-24.

Erasmus, J., Cook, P. A. and Sweijd, N. (1994). Internal shell structure and growth lines in the shell of the abalone, Haliotis midae. *Journal of Shellfish Research*, *13*(2), 493-502.
Evans, A. G., Suo, Z., Wang, R. Z., Aksay, I. A., He, M. Y. and Hutchinson, J. W. (2001). Model for the robust mechanical behavior of nacre. *Journal of Materials Research*, *16*(09), 2475-2484.

Fan, S. and Yilong, B. (2001). Mineral bridges of nacre and its effects. *Acta Mechanica Sinica*, *17*(3), 251-257.

Ghosh, P., Katti, D. R. and Katti, K. S. (2007). Mineral proximity influences mechanical response of proteins in biological mineral-protein hybrid systems. *Biomacromolecules*, *8*(3), 851-856.

Integrated Taxonomic Information System. Haliotis rufescens. Retrieved May 9, 2016, from http://www.itis.gov/servlet/SingleRpt/SingleRpt?search_topic=TSN&search_value=694977

Jackson, A. P., Vincent, J. F. V. and Turner, R. M. (1988). The mechanical design of nacre. *Proceedings of the Royal Society of London B: Biological Sciences*, *234*(1277), 415-440.

Ji, B. and Gao, H. (2004). Mechanical properties of nanostructure of biological materials. *Journal of the Mechanics and Physics of Solids*, *52*(9), 1963-1990.

Katti, D. R., Katti, K. S., Sopp, J. M. and Sarikaya, M. (2001). 3D finite element modeling of mechanical response in nacre-based hybrid nanocomposites. *Computational and Theoretical Polymer Science*, *11*(5), 397-404.

Katti, K. S. and Katti, D. R. (2006). Why is nacre so tough and strong?. *Materials Science and Engineering: C*, *26*(8), 1317-1324.

Katti, K. S., Katti, D. R., Pradhan, S. M. and Bhosle, A. (2005). Platelet interlocks are the key to toughness and strength in nacre. *Journal of Materials Research*, *20*(05), 1097-1100.

Kotha, S. P., Li, Y. and Guzelsu, N. (2001). Micromechanical model of nacre tested in tension. *Journal of materials science*, *36*(8).

Li, X., Xu, Z. H. and Wang, R. (2006). In situ observation of nanograin rotation and deformation in nacre. *Nano letters*, *6*(10), 2301-2304.

Lin, A. Y. M. and Meyers, M. A. (2005). Growth and structure in abalone shell. *Materials Science and Engineering: A*, *390*(1), 27-41.

Lin, A. Y. M. (2008). *Structural and functional biological materials: abalone nacre, sharp materials, and abalone foot adhesion*. ProQuest.

Lin, A. Y. M., Chen, P. Y. and Meyers, M. A. (2008). The growth of nacre in the abalone shell. *Acta biomaterialia*, *4*(1), 131-138.

Lin, A. Y. M. and Meyers, M. A. (2009). Interfacial shear strength in abalone nacre. *Journal of the mechanical behavior of biomedical materials*, *2*(6), 607-612.

Menig, R., Meyers, M. H., Meyers, M. A. and Vecchio, K. S. (2000). Quasi-static and dynamic mechanical response of Haliotis rufescens (abalone) shells. *Acta Materialia*, *48*(9), 2383-2398.

Meyers, M. A., Lin, A. Y. M., Chen, P. Y. and Muyco, J. (2008). Mechanical strength of abalone nacre: role of the soft organic layer. *Journal of the Mechanical behavior of biomedical materials*, *1*(1), 76-85.

Okumura, K. and De Gennes, P. G. (2001). Why is nacre strong? Elastic theory and fracture mechanics for biocomposites with stratified structures. *The European Physical Journal E*, *4*(1), 121-127.

Rosario Beach Marine Laboratory. Encyclopedia of life - Haliotis rufescens, 2011. Retrieved July 12, 2016, from http://eol.org/pages/620396/details

Sanctuary Integrated Monitoring Network. (n.d.). Retrieved June 10, 2016, from http://sanctuarysimon.org/news/2013/07/fish-and-game-commission-acts-to-protect-red-abalone/

Sarikaya, M. (1994). An introduction to biomimetics: a structural viewpoint. *Microscopy research and technique*, *27*(5), 360-375.

Sarikaya, M., Aksay, I. A. and Case, S. (1992). *Results and problems in cell differentiation in biopolymers* (Doctoral dissertation, ed. S. Case (Amsterdam: Springer Verlag, 1992)).

Sarikaya, M., Gunnison, K. E., Yasrebi, M. and Aksay, I. A. (1989). Mechanical property-microstructural relationships in abalone shell. In *MRS proceedings* (Vol. 174, p. 109). Cambridge University Press.

Shenoi, B. A. (2005). *Introduction to digital signal processing and filter design/ B. A. Shenoi*. New York, NY, United States: John Wiley & Sons..

Soldati, A. L., Jacob, D. E., Glatzel, P., Swarbrick, J. C. and Geck, J. (2016). Element substitution by living organisms: the case of manganese in mollusc shell aragonite. *Scientific reports*, *6*.

Song, F., Soh, A. K. and Bai, Y. L. (2003). Structural and mechanical properties of the organic matrix layers of nacre. *Biomaterials*, *24*(20), 3623-3631.

Song, F., Zhang, X. H. and Bai, Y. L. (2002). Microstructure and characteristics in the organic matrix layers of nacre. *Journal of materials research*, *17*(07), 1567-1570.

Su, X., Belcher, A. M., Zaremba, C. M., Morse, D. E., Stucky, G. D. and Heuer, A. H. (2002). Structural and microstructural characterization of the growth lines and prismatic microarchitecture in red abalone shell and the microstructures of abalone "flat pearls". *Chemistry of Materials*, *14*(7), 3106-3117.

Sumitomo, T., Kakisawa, H. and Kagawa, Y. (2011). Nanoscale structure and mechanical behavior of growth lines in shell of abalone Haliotis gigantea. *Journal of structural biology*, *174*(1), 31-36.

Sumitomo, T., Kakisawa, H., Owaki, Y. and Kagawa, Y. (2008). In situ transmission electron microscopy observation of reversible deformation in nacre organic matrix. *Journal of Materials Research*, *23*(05), 1466-1471.

Sun, J., & Bhushan, B. (2012). Hierarchical structure and mechanical properties of nacre: a review. *Rsc Advances*, *2*(20), 7617-7632.

Tan, T., Ren, F., Wang, J. J. A., Lara-Curzio, E., Agastra, P., Mandell, J. and LaFrance, C. M. (2013). Investigating fracture behavior of polymer and polymeric composite materials using spiral notch torsion test. *Engineering Fracture Mechanics*, *101*, 109-128.

University of California. Pacific Rocky Intertidal Monitoring: Trends and Synthesis Retrieved February 13, 2016, from http://www.eeb.ucsc.edu/pacificrockyintertidal/target/target-species-haliotis-rufescens.html

Wang, J. A. J. (2003). Oak Ridge National Laboratory (ORNL) spiral notch torsion test (SNTT) system. *Practical Failure Analysis*, *3*(4), 23-27.

Wegst, U. G. K. and Ashby, M. F. (2004). The mechanical efficiency of natural materials. *Philosophical Magazine*, *84*(21), 2167-2186.

Weiner, S. (1979). Aspartic acid-rich proteins: major components of the soluble organic matrix of mollusk shells. *Calcified Tissue International*, *29*(1), 163-167.